

A finite element procedure for radio-frequency sheath-plasma interactions based on a sheath impedance model

H. Kohno

Kyushu Institute of Technology

J.R. Myra

Lodestar Research Corporation

June 2017

accepted for publication in *Computer Physics Communications*

DOE-ER/54823-21

LRC-17-172

LODESTAR RESEARCH CORPORATION

2400 Central Avenue
Boulder, Colorado 80301

A finite element procedure for radio-frequency sheath-plasma interactions based on a sheath impedance model

H. Kohno^{a,*}, J.R. Myra^b

^a*Department of Mechanical Information Science and Technology, Kyushu Institute of Technology, 680-4 Kawazu, Izuka, Fukuoka 820-8502, Japan*

^b*Lodestar Research Corporation, 2400 Central Avenue P-5, Boulder, CO 80301, USA*

Abstract

A finite element code that solves self-consistent radio-frequency (RF) sheath-plasma interaction problems is improved by incorporating a generalized sheath boundary condition in the macroscopic solution scheme. This sheath boundary condition makes use of a complex sheath impedance including both the sheath capacitance and resistance, which enables evaluation of not only the RF voltage across the sheath but also the power dissipation in the sheath. The newly developed finite element procedure is applied to cases where the background magnetic field is perpendicular to the sheath surface in one- and two-dimensional domains filled by uniform low- and high-density plasmas. The numerical results are compared with those obtained by employing the previous capacitive sheath model at a typical frequency for ion cyclotron heating used in fusion experiments. It is shown that for sheaths on the order of 100 V in a high-density plasma, localized RF power deposition can reach a level which causes material damage. It is also shown that the sheath-plasma wave resonances predicted by the capacitive sheath model do not occur when parameters are such that the generalized sheath impedance model substantially modifies the capacitive character of the sheath. Possible explanations for the difference in the maximum RF sheath voltage depending on the plasma density are also discussed.

*Corresponding author

Email addresses: kohno@mse.kyutech.ac.jp (H. Kohno), jrmyra@lodestar.com (J.R. Myra)

Keywords: Plasma waves, Radio-frequency sheaths, Plasma-surface interactions, Cold plasma, Magnetic confinement fusion, Finite element method

1. Introduction

Radio-frequency (RF) sheaths form when RF waves, plasma, and material surfaces coexist. RF sheaths are important in many situations including plasma processing devices [1–4], magnetic fusion devices [5–18], and plasma science experiments [19, 20]. In the area of magnetic fusion, RF sheaths have mostly been studied in the ion cyclotron range of frequencies (ICRF) in the context of heating and current drive in tokamaks. In this frequency range, it is believed that sheath effects may often be important in limiting successful operation through enhanced impurity sputtering. However, sheath effects in other frequency ranges may also be of interest. As explained subsequently, the properties of RF interactions with the sheath are in part controlled by the dimensionless ratio of the wave to ion plasma frequency, $\omega/\omega_{\text{pi}}$, independent of the absolute frequency band. Finally, an understanding of RF sheaths arising from waves in any of these regimes is of interest for interpretation of diagnostic Langmuir probe signals when those probes are used in an RF environment [14].

The problem of solving for global wave behavior in a plasma volume that is bounded by material surfaces, and hence RF sheaths, involves multi-scale physics. The sheath physics takes place on the scale of the electron Debye length which is many orders of magnitude smaller than typical RF wavelengths, or plasma dimensions of interest. In order to alleviate computational issues associated with the large disparity in space scales, a useful procedure has been to mathematically separate the microscopic sheath and macroscopic plasma volume (i.e., RF wave propagation) problems.

From the point of view of the macroscopic problem considered in this paper, the sheath physics will be collapsed into a sheath boundary condition (sheath BC) on the surface. This boundary condition describes the electromagnetic interaction of the waves with the boundary in terms of a surface impedance. Various implementations of a sheath boundary have been devised in previous work [2, 6, 8, 18, 21, 22] and in the numerical code “rfSOL” developed by the authors [16, 23, 24]; however, these studies have been restricted to or focused on the capacitive sheath regime, where the complex sheath impedance is purely imaginary. Here, we consider the solution of the

wave propagation problem using a recently available formulation of the *generalized* sheath impedance [25, 26]. The generalized sheath impedance is fully complex with both real and imaginary parts that describe both resistive and capacitive physics. This model allows calculation of not only the rectified sheath potential (important for ion sputtering impact energies), but also the RF power dissipation in the sheath. Because the solution of the wave propagation problem in the volume must be self-consistent with the boundary condition, it is expected that the generalized sheath impedance model can lead to significantly different predictions than the capacitive sheath model in some parameter regimes.

Our objective in this paper is to present a new finite element scheme for analyzing RF sheath-plasma interactions to evaluate the RF voltage across the sheath and the sheath power dissipation accurately over interesting parameter ranges in the RF voltage and normalized frequency $\hat{\omega} = \omega/\omega_{pi}$. The proposed numerical scheme can be regarded as a micro-macro decoupling scheme in which the accuracy of the macroscopic solution is assured by including the microscopic sheath physics (i.e., the dynamics of the time-dependent magnetic presheath and non-neutral Debye sheath [25]) in the sheath BC. The oblique angle magnetized RF sheath considered in Ref. [25] requires four dimensionless parameters to describe the interaction. In this paper, we restrict our attention to the special case of “perpendicular sheaths”, i.e., sheaths where the background magnetic field is perpendicular to the surface. In this special case, only two dimensionless parameters are required; namely, $\hat{\omega}$ and a normalized RF amplitude \tilde{V}_{RF} (which will be defined in Section 2). The sheath impedance parameter is expressed with the use of differentiable functions of these dimensionless parameters in order to apply the Newton–Raphson method to solve the nonlinear system of discretized equations.

The paper is organized as follows. In Section 2, we describe the equations used for simulations of macroscopic RF sheath-plasma interactions. Section 3 presents the finite element procedure with emphasis on incorporation of the discretized sheath BC and current-voltage relation into a system of discretized equations. The validity of the proposed finite element scheme is verified through comparison with an analytical solution in a one-dimensional (1D) closed domain in Section 4. A comparison of the results obtained by the previous and newly developed codes in the capacitive sheath limit is also discussed. Further, numerical results for sheath-plasma interaction problems in a two-dimensional (2D) slab domain filled by low- and high-density plas-

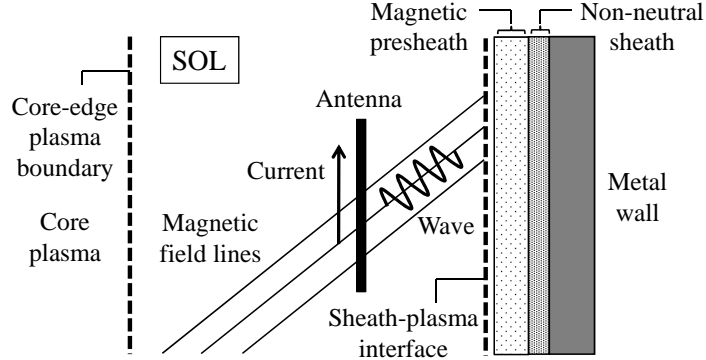


Figure 1: Schematic diagram of a tokamak poloidal cross-section near the antenna, in which the interaction between the sheath and the wave in a cold plasma occurs. Note that the calculation domain bounded by the dashed lines is the same as that shown in Ref. [23], but the magnetic presheath is introduced in the new sheath model.

mas are presented in Section 5. Lastly, conclusions of the present work are described in Section 6.

2. Formulation for RF sheath-plasma interactions based on a sheath impedance model

This section summarizes the equations that govern the behavior of plasma waves and the macroscopic interaction between the waves and the sheaths on metal surfaces. Fig. 1 shows a simplified schematic of the tokamak poloidal cross-section in the vicinity of a limiter or other vessel surface. It is assumed that the magnetic field lines intersect with a metal surface and thereby the sheath, which consists of the non-neutral sheath and magnetic presheath. The region investigated in this numerical study is the scrape-off layer (SOL) bounded by the two dashed lines in Fig. 1, namely, the core-edge plasma boundary and sheath-plasma interface. (In this and the following sections, the hypothetical boundary surface between the magnetic presheath and the plasma is abbreviated to the sheath surface or sheath-plasma interface.) Note that the physics inside the sheath is not solved by the present numerical code but has influence on the macroscopic simulation through the sheath BC, as described later. All the analyses in this study will be conducted using a cold plasma model, which is typically valid due to low plasma temperatures (~ 10 eV). Also, we assume that only deuterium is considered as an ion species, so that the ion mass is $m_i = 3.3436 \times 10^{-27}$ kg.

The governing equation for plasma waves in the SOL is a combined form of Maxwell's equations described as

$$\nabla \times \nabla \times \mathbf{E} - \frac{\omega^2}{c^2} \boldsymbol{\epsilon} \cdot \mathbf{E} - i\omega\mu_0 \mathbf{J}_{\text{ext}} = \mathbf{0}, \quad (1)$$

where the electric field \mathbf{E} and the external current \mathbf{J}_{ext} vary on the RF time scale. Here, i is the imaginary unit, ω is the applied angular frequency (waves vary in time t as $e^{-i\omega t}$), and c is the speed of light, having a relation with the dielectric constant ϵ_0 and the permeability μ_0 in vacuum, which is expressed as $c^2 = (\epsilon_0\mu_0)^{-1}$. The dielectric tensor $\boldsymbol{\epsilon}$ is given based on the cold plasma model (see Ref. [23] for the definitions including the dielectric tensor components ϵ_{\perp} , ϵ_{\parallel} , and ϵ_{\times}). Throughout this study, we assume that quasi-neutrality is retained in the SOL, i.e., $n_{e0} = n_{i0} = n_0$, where n_e and n_i are the number densities of electrons and ions, respectively, and the subscript 0 denotes an equilibrium quantity.

In the present numerical analysis, the sheath-plasma interaction is taken into account by means of a sheath BC proposed in Ref. [25]. First, the general form of the sheath BCs, including the previously used capacitive sheath BC [22], is written as

$$\mathbf{E}_t = -\nabla_t V_{\text{RF}}, \quad (2)$$

where the subscript t denotes the component tangential to the boundary, and V_{RF} is the instantaneous RF voltage across the sheath (hereafter, simply called the RF sheath voltage), which is defined as

$$V_{\text{RF}} \equiv \Phi_{\omega}^{(\text{sh})} \Big|_{\text{s-p interface}} - \Phi_{\omega}^{(\text{sh})} \Big|_{\text{w-s interface}}. \quad (3)$$

Here, $\Phi_{\omega}^{(\text{sh})}$ is the electrostatic potential in the sheath at the frequency ω , which is evaluated at the locations designated in the subscripts; s-p and w-s stand for sheath-plasma and wall-sheath, respectively, and the contributions of the higher harmonics to the RF sheath voltage are neglected as being small. Note that for $V_{\text{RF}} \rightarrow 0$, or equivalently when the sheath width approaches zero, the sheath BC reduces to the conducting-wall boundary condition (conducting-wall BC), $\mathbf{E}_t = \mathbf{0}$. The RF sheath voltage can also be expressed by employing the sheath impedance parameter z_{sh} as

$$V_{\text{RF}} = -J_n^{(\text{sh})} z_{\text{sh}} = -J_n^{(\text{pl})} z_{\text{sh}} = -\frac{\omega}{i} D_n^{(\text{pl})} z_{\text{sh}}, \quad (4)$$

where the superscripts (sh) and (pl) denote quantities on the sheath and plasma sides of the sheath-plasma interface, respectively, $J_n (= \mathbf{s} \cdot \mathbf{J})$ is the component of the total current density \mathbf{J} normal to the sheath surface, and $D_n (= \mathbf{s} \cdot (\varepsilon_0 \boldsymbol{\epsilon} \cdot \mathbf{E}))$ is the component of the electric displacement \mathbf{D} normal to the sheath surface (and \mathbf{s} in the definitions is the unit normal vector pointing into the plasma). In the derivation of Eq. (4), continuity of J_n (or D_n) at the sheath-plasma interface and the fact that the total $J_n^{(\text{sh})}$, including particle and displacement currents, is constant inside the sheath are taken into account [25]. In general, the sheath impedance parameter z_{sh} is a function of four dimensionless parameters which are evaluated on the sheath surface: $\hat{\Omega} = \Omega_i/\omega_{\text{pi}}$, $|b_n|$ (where $b_n = \mathbf{b} \cdot \mathbf{s}$), $\hat{\omega} = \omega/\omega_{\text{pi}}$, and $\tilde{V}_{\text{RF}} = e|V_{\text{RF}}|/T_e$, where Ω_i is the ion cyclotron frequency, ω_{pi} is the ion plasma frequency, \mathbf{b} is the unit vector along the background magnetic field \mathbf{B}_0 (i.e., $\mathbf{b} = \mathbf{B}_0/|\mathbf{B}_0|$), e is the elementary charge, and T_e is the electron temperature. The basic strategy is to pre-calculate z_{sh} through a fully nonlinear fluid micro-scale model and store the results in interpolation functions or approximation fits which are efficient for calculations using the rfSOL code. A simplified example of the approximation fits is shown in Appendix A.

The total sheath voltage V_{total} consists of the RF wave contribution V_{RF} and the rectified sheath voltage V_{rect} , i.e., $V_{\text{total}} = V_{\text{RF}} + V_{\text{rect}}$. Here, V_{rect} is determined by the numerical solution of the microscopic sheath model, and the physics of the microscopic sheath model shows that V_{rect} increases with $|V_{\text{RF}}|$ [25]. Of course, by definition, the time average of V_{total} is equal to V_{rect} .

In order to exclude the core or distant SOL regions from the calculation domain, we introduce a damping layer in the vicinity of the core-edge plasma boundary so as to satisfy an outgoing wave condition, i.e., an absorbing boundary condition (absorbing BC). The method is described in our previous work [23, 24].

3. Finite element discretization

In this section, we consider the discretization for the present formulation in a 2D domain (filled by a cold plasma) subject to the sheath and absorbing BCs. We aim at obtaining a system of equations to be solved for the unknown nodal values of the electric field components and RF sheath voltage in the Cartesian coordinate system. The numerical technique employed for the discretization of the sheath BC may be compared with that described in Section 3.3 of Ref. [23], with V_{RF} now playing the role of $-\Delta_{\text{sh}} D_n/\varepsilon_0$ (where

Δ_{sh} is the time-averaged sheath width) in that paper. A main difference from the previous scheme is the inclusion of the current-voltage relation, Eq. (4), to additionally obtain the RF sheath voltage as a part of the numerical solution.

First, a combined form of Maxwell's equations, Eq. (1), is discretized in the 2D calculation domain Ω based on the standard Galerkin approach. Since the details of this discretization procedure, together with the discretization of the antenna current, are described in the authors' previous paper [23], they will not be repeated here. We only note that a single Fourier mode of the electric field in the z direction and in time is considered in this study and is expressed in the entire domain as

$$\mathbf{E} = \hat{\mathbf{E}}_i N_i(x, y) e^{i(k_z z - \omega t)}, \quad (5)$$

where N_i is the piecewise biquadratic interpolation function and $\hat{\mathbf{E}}_i$ is the vector quantity at node i ; the subscript i denotes the global node number. The summation convention applies to the subscript i . Further, k_z is the z component of the wave vector \mathbf{k} . (Hereafter, the subscripts x , y , and z denote the x , y , and z components of vector quantities, respectively.)

Next, the sheath BC described in Eq. (2) is discretized by employing a 1D finite element method in a manner similar to that of Ref. [23]. Forming the inner product of Eq. (2) with the weight function \mathbf{W}^S , and then integrating it over the sheath surface Γ^S yields

$$\int_{\Gamma^S} \mathbf{W}^S \cdot (\mathbf{E}_t + \nabla_t V_{\text{RF}}) d\Gamma^S = 0. \quad (6)$$

It is assumed here that Γ^S is given as a simple closed curve or a periodic region. Let us next define the weight function, electric field, and RF sheath voltage on Γ^S as

$$\mathbf{W}^S = \hat{\mathbf{W}}_{i'}^S N_{i'}^S(\tau) e^{-ik_z z} = \hat{\mathbf{W}}_{i'}^S \tilde{N}_{i'}^S, \quad (7)$$

$$\mathbf{E} = \hat{\mathbf{E}}_{j'}^S N_{j'}^S(\tau) e^{i(k_z z - \omega t)}, \quad (8)$$

$$V_{\text{RF}} = \hat{V}_{\text{RF}, j'}^S N_{j'}^S(\tau) e^{i(k_z z - \omega t)}, \quad (9)$$

where $N_{i'}^S$ and $N_{j'}^S$ are the piecewise quadratic interpolation functions with respect to τ (the tangential coordinate defined along the sheath surface on the x - y plane), and the subscripts i' and j' denote the node number redefined on Γ^S , which means that the number is different from the global node number assigned to each node in the calculation domain Ω ; $\hat{\mathbf{W}}_{i'}^S$ and $\hat{\mathbf{E}}_{j'}^S$ are the

vector quantities at nodes i' and j' , and $\hat{V}_{\text{RF},j'}$ is the scalar quantity at node j' . Here the summation convention applies to the subscripts i' and j' , and the superscript S is attached to explicitly show that the quantity is positioned on Γ^{S} . The interpolation function $N_{i'}^{\text{S}}$ or $N_{j'}^{\text{S}}$ is locally defined in a 1D three-node element on the sheath surface. Since Eq. (6) needs to be satisfied for arbitrary weight functions, we obtain

$$\int_{\Gamma^{\text{S}}} \tilde{N}_{i'}^{\text{S}} \left(E_{\tau} + \frac{\partial V_{\text{RF}}}{\partial \tau} \right) d\Gamma^{\text{S}} = 0, \quad (10)$$

$$\int_{\Gamma^{\text{S}}} \tilde{N}_{i'}^{\text{S}} (E_z + ik_z V_{\text{RF}}) d\Gamma^{\text{S}} = 0, \quad (11)$$

considering that $V_{\text{RF}} \propto e^{ik_z z}$. The corresponding discretized equations are obtained by substituting Eqs. (8) and (9) into Eqs. (10) and (11) as follows:

$$G_{\tau i'} \equiv [N_{i'}^{\text{S}} N_{j'}^{\text{S}}] \hat{E}_{\tau j'}^{\text{S}} + [N_{i'}^{\text{S}} \check{N}_{j'}^{\text{S}}] \hat{V}_{\text{RF},j'} = 0, \quad (12)$$

$$G_{z i'} \equiv [N_{i'}^{\text{S}} N_{j'}^{\text{S}}] \hat{E}_{z j'}^{\text{S}} + ik_z [N_{i'}^{\text{S}} N_{j'}^{\text{S}}] \hat{V}_{\text{RF},j'} = 0, \quad (13)$$

where

$$[N_{i'}^{\text{S}} N_{j'}^{\text{S}}] \equiv \int_{\Gamma^{\text{S}}} N_{i'}^{\text{S}} N_{j'}^{\text{S}} d\Gamma^{\text{S}}, \quad [N_{i'}^{\text{S}} \check{N}_{j'}^{\text{S}}] \equiv \int_{\Gamma^{\text{S}}} N_{i'}^{\text{S}} \frac{dN_{j'}^{\text{S}}}{d\tau} d\Gamma^{\text{S}}. \quad (14)$$

The tangential component of $\hat{\mathbf{E}}_{j'}^{\text{S}}$ is expressed by $\hat{E}_{\tau j'}^{\text{S}} = \mathbf{e}_x \cdot \mathbf{e}_{\tau j'} \hat{E}_{x j'}^{\text{S}} + \mathbf{e}_y \cdot \mathbf{e}_{\tau j'} \hat{E}_{y j'}^{\text{S}}$, where \mathbf{e}_x and \mathbf{e}_y are the unit vectors in the x and y directions, respectively, and $\mathbf{e}_{\tau j'}$ is the unit vector in the τ direction at node j' .

The current-voltage relation shown in Eq. (4) need not be discretized, since it does not include any differential operators. At node i' on the sheath surface, this relation is expressed as

$$H_{i'} \equiv \hat{V}_{\text{RF},i'} - i\varepsilon_0 \omega z_{\text{sh},i'} \left(\mathbf{s}_{i'} \cdot \boldsymbol{\epsilon}_{i'}^{\text{S}} \cdot \hat{\mathbf{E}}_{i'}^{\text{S}} \right) = 0, \quad (15)$$

which is obtained by employing $V_{\text{RF},i'} = \hat{V}_{\text{RF},i'} e^{i(k_z z - \omega t)}$ and $\mathbf{E}_{i'} = \hat{\mathbf{E}}_{i'}^{\text{S}} e^{i(k_z z - \omega t)}$ (see Eqs. (8) and (9)). Evidently, in contrast to the approach in Refs. [16, 23], there is no need to interpolate the dielectric tensor $\boldsymbol{\epsilon}$ on the sheath surface.

The resultant nonlinear system of equations can be solved by employing the Newton–Raphson method. The procedure is described in Appendix B. For the calculations in 2D domains, the system of linear equations at

each Newton–Raphson iteration is computed by employing MUMPS (Multifrontal Massively Parallel sparse direct Solver) on the Edison (Cray XC30) computer system at the National Energy Research Scientific Computing Center (NERSC).

4. Verification of the scheme for sheath-plasma interactions in 1D geometry

In order to verify the validity of the developed finite element scheme for sheath-plasma interactions, we first derive an analytical solution for the RF wave field and sheath voltage in 1D geometry under the condition where the direction of a constant background magnetic field is perpendicular to the sheath surfaces. Then, we compare a numerical solution with an analytical solution under a low-density plasma condition. We also investigate how the present sheath impedance model relates to the previous capacitive sheath model. Our focus in this paper is on understanding fundamental sheath interactions with waves; the parameters chosen in this section (and in the next section) are similar to ICRF, edge and SOL parameters in tokamaks although we do not attempt to model any specific experiment here. The analytical and numerical results shown in Sections 4.2 and 4.3 are assumed to be on the plane of $y = z = 0$ m at $t = 2\pi l/\omega$, where l is an integer.

4.1. Analytical solution for constant n_0 and \mathbf{B}_0

The calculation domain considered here is shown in Fig. 2; a constant-density plasma is filled in a waveguide which is assumed to be infinitely long in the y and z directions. This calculation model is the same as the one used for the derivation of an analytical solution in Ref. [23]. The background magnetic field is also assumed to be constant in magnitude and is pointed purely in the x direction. The wave vector components k_y and k_z are fixed, and the antenna current density is given by

$$\mathbf{J}_{\text{ext}} = K \delta(x - x_{\text{ant}}) e^{i(k_y y + k_z z - \omega t)} \mathbf{e}_y, \quad (16)$$

where K is constant.

Now, let us look for a solution to Eq. (1) in the form $\mathbf{E} = \bar{\mathbf{E}} e^{i(k_x x + k_y y + k_z z - \omega t)}$. Then, we obtain the dispersion relation that forms a quadratic equation in terms of k_x^2 . Since the domain is divided by the presence of the external

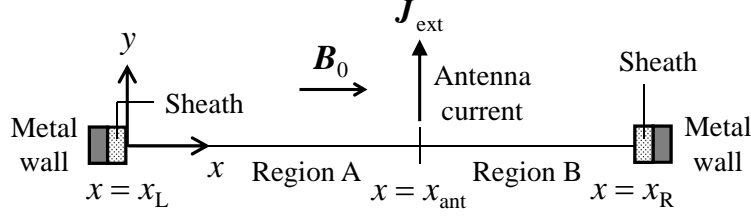


Figure 2: Sheath-plasma interaction problem defined on the 1D domain including the antenna current and bounded by the sheaths on both sides; this 1D calculation model was also used in Ref. [23].

surface current, the general solutions for the electric field in region A and region B in Fig. 2 are, respectively, written as

$$\mathbf{E}_A = \hat{\mathbf{E}}_A(x) e^{i(k_y y + k_z z - \omega t)}, \quad \mathbf{E}_B = \hat{\mathbf{E}}_B(x) e^{i(k_y y + k_z z - \omega t)}, \quad (17)$$

where

$$\hat{\mathbf{E}}_A(x) \equiv \sum_{j=1}^4 C_{Aj} \tilde{\mathbf{E}}_j e^{ik_{xj} x}, \quad \hat{\mathbf{E}}_B(x) \equiv \sum_{j=1}^4 C_{Bj} \tilde{\mathbf{E}}_j e^{ik_{xj} x}. \quad (18)$$

Here, C_{A1}, \dots, C_{A4} and C_{B1}, \dots, C_{B4} are constants to be determined, and $\tilde{\mathbf{E}}_1, \dots, \tilde{\mathbf{E}}_4$ are the polarization eigenvectors corresponding to k_{x1}, \dots, k_{x4} , respectively. The subscripts A and B denote the regions where the quantities are defined. The expressions for the RF sheath voltage at $x = x_L$ and $x = x_R$ are, respectively, given by

$$V_{\text{RF}}|_{x=x_L} = \hat{V}_A e^{i(k_y y + k_z z - \omega t)}, \quad V_{\text{RF}}|_{x=x_R} = \hat{V}_B e^{i(k_y y + k_z z - \omega t)}. \quad (19)$$

Since the magnetic field line intersects at a right angle with the walls, the sheath must be present at both ends, which yields the following four conditions:

$$\begin{aligned} \hat{E}_{Ay}(x_L) &= -ik_y \hat{V}_A, & \hat{E}_{Az}(x_L) &= -ik_z \hat{V}_A, \\ \hat{E}_{By}(x_R) &= -ik_y \hat{V}_B, & \hat{E}_{Bz}(x_R) &= -ik_z \hat{V}_B. \end{aligned} \quad (20)$$

Further, the current-voltage relations at both ends are written as

$$\hat{V}_A = -\frac{\omega}{i} \hat{D}_{Ax} z_{\text{sh}} \Big|_{x=x_L}, \quad \hat{V}_B = -\frac{\omega}{i} \hat{D}_{Bx} z_{\text{sh}} \Big|_{x=x_R}, \quad (21)$$

where $\hat{D}_{Ax} = \varepsilon_0 \varepsilon_{xx} \hat{E}_{Ax}$ and $\hat{D}_{Bx} = -\varepsilon_0 \varepsilon_{xx} \hat{E}_{Bx}$; ε_{xx} is a dielectric tensor component. At the position where the surface current is present ($x = x_{\text{ant}}$), one has to consider the jump conditions in both the electric and magnetic fields, which gives four additional equations (see Section 4.1 of Ref. [23]). Consequently, one finds that the problem can be analytically solved, since the number of unknowns is the same as the number of equations (i.e., the number is 20 when we decompose the unknowns and equations into their real and imaginary parts). Due to the nonlinearity in the sheath BCs at both ends, one has to iteratively calculate the system of equations to obtain the constants C_{Aj} , C_{Bj} ($j = 1, \dots, 4$), \hat{V}_A , and \hat{V}_B , for example, using the Newton–Raphson method.

4.2. Comparison between the analytical and numerical solutions

First of all, a numerical solution is obtained with the newly developed rfSOL code for a 1D domain. This 1D code is straightforwardly constructed by noting that $\partial/\partial\tau$ is equivalent to ik_y in the sheath BCs at both ends and the integrations over the sheath surface Γ^S (for the spatial discretization) are not necessary. The result from the 1D code is compared with the analytical solution given in Section 4.1. Based on Fig. 2, the calculation domain is defined such that $x_L = 0$ m, $x_{\text{ant}} = 0.8$ m, and $x_R = 1$ m. The plasma density and background magnetic field are assumed to be constant; $n_0 = 3 \times 10^{17}$ m $^{-3}$ and $B_0 = B_{0x} = 1$ T (where $B_0 = |\mathbf{B}_0|$). The other parameters fixed in this analysis are $T_e = 15$ eV, $f = 80$ MHz (where $\omega = 2\pi f$), $k_y = 0$ m $^{-1}$, $k_z = 10.8$ m $^{-1}$, and $K = 560$ A/m. A uniform mesh which includes 201 nodes (100 three-node elements) is used for the finite element discretization.

Fig. 3 shows the comparison of the analytically and numerically calculated profiles of the electric field components, which are obtained by imposing the generalized sheath BC at $x = x_L$ and $x = x_R$, together with the profiles obtained subject to the conducting-wall BC which corresponds to the case for $T_e = 0$ eV. (The sheath BC is abbreviated as SBC in the graph legends. This abbreviation will also be used in Section 5.) It is confirmed in Fig. 3(a) and (b) that the profiles obtained by the 1D rfSOL code are in good agreement with the exact profiles of these electric field components when the sheaths are present on both sides of the domain. Note that $\text{Re}(E_x) = 0$ V/m in the entire domain when the sheaths are not present on the metal walls. In addition, although not shown here, $\text{Re}(E_x) = 0$ V/m and nonzero $\text{Im}(E_x)$ are still obtained even if the conducting-wall BC is replaced with the previously used capacitive sheath BC; in both of these cases, E_x is $\pi/2$ out of phase with

the y component of the antenna current density, $J_{\text{ext},y}$. Good agreement is also confirmed in the RF sheath voltage values at both ends. The absolute values of the nonzero RF sheath voltage at $x = x_L$ and $x = x_R$, which are expressed as $|V_{\text{RF}}|_{x=x_L}$ and $|V_{\text{RF}}|_{x=x_R}$, are 25.41 V and 101.73 V in the analytical solution, respectively; on the other hand, $|V_{\text{RF}}|_{x=x_L} = 25.41$ V and $|V_{\text{RF}}|_{x=x_R} = 101.80$ V in the numerical solution. Having verified the new code using the analytical solution, in the next subsection, we will show the comparison of the analytical solutions obtained under the capacitive and generalized sheath BCs.

4.3. Relation between the capacitive and generalized sheath BCs

In the capacitive sheath limit, the dimensionless sheath admittance parameter (the inverse of the dimensionless sheath impedance parameter \hat{z}_{sh}) is expressed only by the dimensionless displacement current admittance parameter as follows (see Eq. (A.9) in Appendix A):

$$\frac{1}{\hat{z}_{\text{sh}}} = -i \frac{\hat{\omega}}{\hat{\Delta}_{\text{sh}}} = -i \frac{\omega \lambda_{\text{De}}}{\Delta_{\text{sh}} \omega_{\text{pi}}}, \quad (22)$$

where $\hat{\Delta}_{\text{sh}}$ is the dimensionless time-averaged sheath width defined as $\hat{\Delta}_{\text{sh}} = \Delta_{\text{sh}}/\lambda_{\text{De}}$; λ_{De} is the electron Debye length defined as $\lambda_{\text{De}} = (\varepsilon_0 T_e / n_{e0} e^2)^{1/2}$. As given in Ref. [25], the dimensionless sheath impedance parameter is converted into the dimensional one through the following relation:

$$z_{\text{sh}} = \frac{\lambda_{\text{De}}}{\varepsilon_0 \omega_{\text{pi}}} \hat{z}_{\text{sh}}. \quad (23)$$

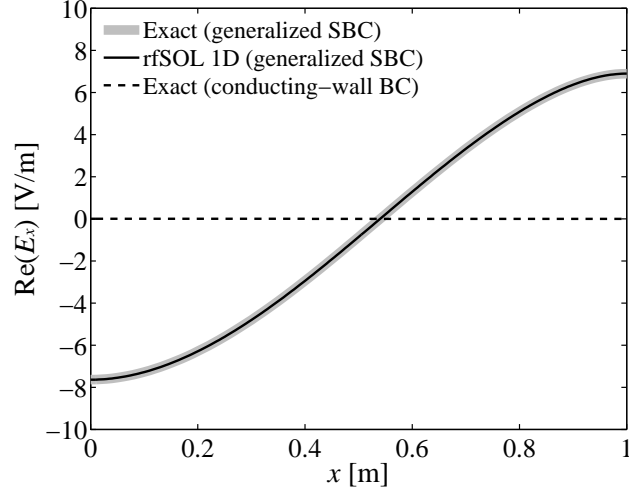
By substituting Eq. (22) into Eq. (23) and then substituting the obtained expression into Eq. (4), the sheath BC shown in Eq. (2) can be rewritten as

$$\mathbf{E}_t = \nabla_t \left(\frac{\Delta_{\text{sh}}}{\varepsilon_0} D_n \right), \quad (24)$$

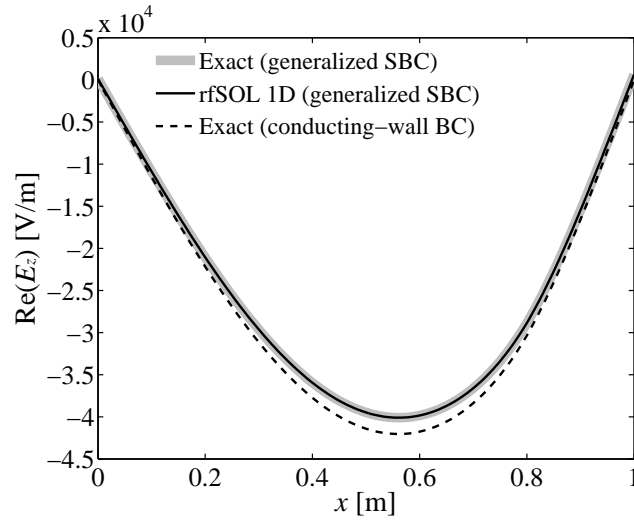
which is identical with the capacitive sheath BC (for $\varepsilon_{\text{sh}} = \varepsilon_0$) derived in Ref. [22] and used in the original rfsOL code [23]. (The superscript (pl) in Eq. (4) is omitted in Eq. (24).)

In the capacitive sheath model, the dimensionless time-averaged sheath width is assumed to satisfy the Child–Langmuir law [27, 28] in the form

$$\hat{\Delta}_{\text{sh}} = \hat{V}_{\text{rect}}^{3/4}, \quad (25)$$



(a)



(b)

Figure 3: Comparison of the entire profiles of $\text{Re}(E_x)$ (a) and $\text{Re}(E_z)$ (b) between the analytical and numerical solutions for $K = 560$ A/m, which are obtained by imposing either the generalized sheath BCs or the conducting-wall BCs at $x = 0$ m and $x = 1$ m.

where \hat{V}_{rect} is the dimensionless rectified (direct-current) sheath voltage. For the present sheath impedance model, the expression for \hat{V}_{rect} is given by Eq. (A.10) with the assumption that the background magnetic field perpendicularly intersects the sheath surface. On the other hand, for the previous capacitive sheath model, the expression for \hat{V}_{rect} is

$$\hat{V}_{\text{rect}} = C_{\text{sh}} \tilde{V}_{\text{RF}} \quad (26)$$

in the strong RF driven sheath regime, where C_{sh} is an order-unity constant giving the rectification factor. Due to the difference in expressions for \hat{V}_{rect} , it is not expected even in the capacitive sheath limit that the numerical solutions satisfying the capacitive sheath BC (i.e., Eq. (24)) completely agree with each other. However, it should be emphasized that the analytical fits used in the sheath impedance model provide a more accurate numerical evaluation.

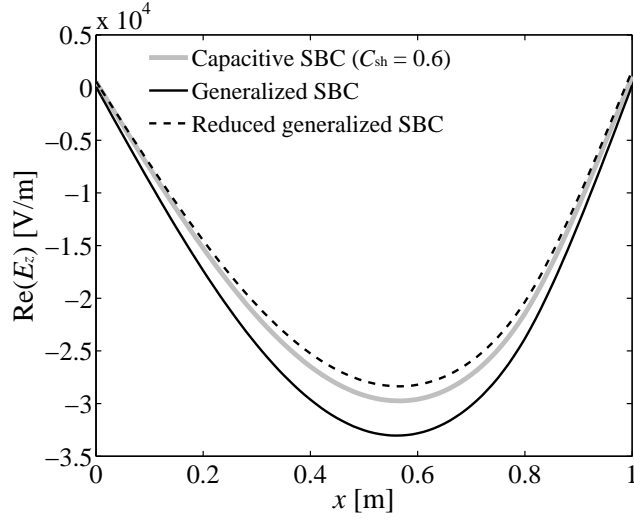
Fig. 4 shows the comparison of the analytically calculated profiles of $\text{Re}(E_z)$ in the three different solutions obtained by imposing the previously used capacitive sheath BC (hereafter, simply called the capacitive sheath BC), generalized sheath BC, and “reduced” generalized sheath BC, in which only the displacement current contribution given by Eq. (A.9) is considered (i.e., the contributions of ions and electrons to the sheath admittance parameter are excluded), at $x = x_L$ and $x = x_R$ shown in Fig. 2. Here, we investigate the following two cases: $n_0 = 3 \times 10^{17} \text{ m}^{-3}$ and $K = 450 \text{ A/m}$ (higher density case) and $n_0 = 1 \times 10^{17} \text{ m}^{-3}$ and $K = 1.5 \text{ kA/m}$ (lower density case). The other parameters used for this analysis remain the same as described in Section 4.2. The analytical solutions satisfying the capacitive sheath BCs at both ends are obtained according to the procedure described in Ref. [23]; here, the rectification factor is taken to be $C_{\text{sh}} = 0.6$. It is seen in Fig. 4(a) that the result satisfying the capacitive sheath BCs is closer to the result satisfying the reduced generalized sheath BCs than that satisfying the generalized sheath BCs. The absolute values of the RF sheath voltage for this higher density case are 52.68 V, 17.95 V, and 54.40 V at $x = x_L$ and 98.98 V, 41.45 V, and 148.06 V at $x = x_R$ when the capacitive sheath BC, generalized sheath BC, and reduced generalized sheath BC are taken into account, respectively. On the other hand, it is seen in Fig. 4(b) that the result satisfying the capacitive sheath BCs is closer to the result satisfying the generalized sheath BCs than that satisfying the reduced generalized sheath BCs, although the differences between these profiles are small. The absolute values of the RF sheath voltage for this lower density case are 26.12

V, 12.72 V, and 22.56 V at $x = x_L$ and 93.85 V, 126.21 V, and 146.04 V at $x = x_R$ when the capacitive sheath BC, generalized sheath BC, and reduced generalized sheath BC are taken into account, respectively. Therefore, it should be noted that the exclusion of the contributions of ions and electrons to the sheath impedance parameter used in the generalized sheath BC does not always make a solution closer to the one given by the capacitive sheath model under the same calculation condition. Also, clearly the RF sheath voltage can be rather sensitive to the boundary condition, motivating the use of the more physically accurate generalized sheath BC. Further investigation reveals that there is a global eigenmode of the computational box near the condition of $n_0 = 3 \times 10^{17} \text{ m}^{-3}$ (with the given parameters), which accounts for the large electric field amplitude in that case (as shown in Fig. 4(a)). A detailed analysis of this 1D problem including the investigation of the dependence of the RF sheath voltage, sheath power absorption, and dimensionless sheath impedance parameter on the antenna current density is described in Ref. [26].

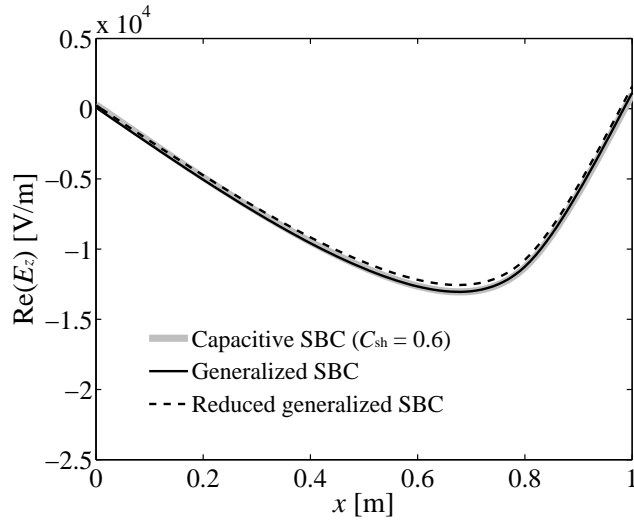
In summary, for the cases investigated in Fig. 4, the solutions in the plasma volume are not strongly dependent on the boundary condition, and all the cases give $\text{Re}(E_z)$ close to zero at the wall. Insensitivity to the boundary condition is not always the case, as will be demonstrated in the next section. However, even when the volume solutions are similar, the RF sheath voltage can be strongly dependent on the boundary condition as noted in the preceding paragraph. This point, as well as the need to model sheath power absorption, is the motivation for employing the generalized sheath BC. It is the main new message of our paper and will be investigated in the next section using a 2D domain.

5. RF sheath-plasma interactions in a semi-infinite 2D slab domain

As a next step, we consider analyzing sheath-plasma interaction problems in 2D slab geometry using the 2D rfSOL codes. Fig. 5 shows the problem definition; here, a combined form of Maxwell's equations is solved subject to the generalized sheath BC (or the capacitive sheath BC for the purpose of comparison) on the right-hand side, the absorbing BC on the left-hand side (if necessary, i.e., in the case where waves propagate to the left boundary), and a periodic boundary condition (periodic BC) that connects the top and bottom of the domain. Based on this geometry and coordinate system, the partial derivative with respect to τ defined in the discretization of the sheath



(a)



(b)

Figure 4: Comparison of the entire profiles of $\text{Re}(E_z)$ between the three different analytical solutions obtained by imposing the capacitive sheath BCs, generalized sheath BCs, and reduced generalized sheath BCs at $x = 0$ m and $x = 1$ m for $n_0 = 3 \times 10^{17} \text{ m}^{-3}$ and $K = 450 \text{ A/m}$ (a) and $n_0 = 1 \times 10^{17} \text{ m}^{-3}$ and $K = 1.5 \text{ kA/m}$ (b).

BC (see Section 3) is equivalent to the partial derivative with respect to y . The antenna surface current is given by using a cosine function in the y direction in the range $(L_y - L_{\text{ant}})/2 \leq y \leq (L_y + L_{\text{ant}})/2$ as follows:

$$\mathbf{J}_{\text{ext}} = K(y) \delta(x - D_{\text{bl-ant}}) e^{i(k_z z - \omega t)} \mathbf{e}_y, \quad (27)$$

where

$$K(y) = K_{\text{max}} \cos^2 \left[\frac{\pi}{L_{\text{ant}}} \left(y - \frac{L_y}{2} \right) \right]. \quad (28)$$

In this analysis, the plasma density and background magnetic field are assumed to be constant over the domain and the background magnetic field is perpendicular to the sheath surface on the right-hand side. The following parameters are fixed throughout the analysis: $L_x = 1.2$ m (horizontal dimension of the domain), $D_{\text{bl-ant}} = 1$ m (distance between the boundary on the left-hand side and the antenna), $L_y = 0.2$ m (vertical dimension or periodic length of the domain), and $L_{\text{ant}} = 0.05$ m (antenna length); $B_{0x} = 1$ T, $B_{0y} = 0$ T, and $B_{0z} = 0$ T for the background magnetic field; $C_{\text{sh}} = 0.6$ used in the capacitive sheath BC; and $T_e = 15$ eV and $f = 80$ MHz. The calculation domain is divided by a non-uniform mesh which includes 800 (in the x direction) \times 200 (in the y direction) nine-node elements (or 1601×401 nodes) in total; 600×200 and 200×200 elements are allocated in $0 \leq x \leq D_{\text{bl-ant}}$ and $D_{\text{bl-ant}} \leq x \leq L_x$, respectively. In this mesh, the nodal positions in the x direction are concentrated in the vicinity of the antenna and sheath surface in order to accurately resolve possible thin layers, within which waves from the antenna and/or sheath-plasma waves (SPWs) exponentially decay. (For example, in addition to the main root of interest in Section 5.1, Eq. (29) also has a large n_{\parallel} root which is strongly evanescent.) The other parameters which have not yet been specified are varied depending on the problems considered below.

5.1. Interactions with propagating waves in a low-density plasma

First, we consider cases where a low-density plasma fills in the 2D slab domain and large values of k_z are prescribed. Here, the plasma density n_0 is fixed at $1 \times 10^{17} \text{ m}^{-3}$, and the calculations are carried out with two different values of k_z : 160 m^{-1} and 320 m^{-1} . In order to avoid the reflection of waves at the boundary on the left-hand side, an absorbing layer is formed with the use of the collision frequency given by $\nu = \nu_0 e^{-x/\lambda_\nu}$ (see Refs. [23, 24]); the parameters used here are $\nu_0 = 3 \times 10^{11} \text{ s}^{-1}$ and $\lambda_\nu = 0.1$ m.

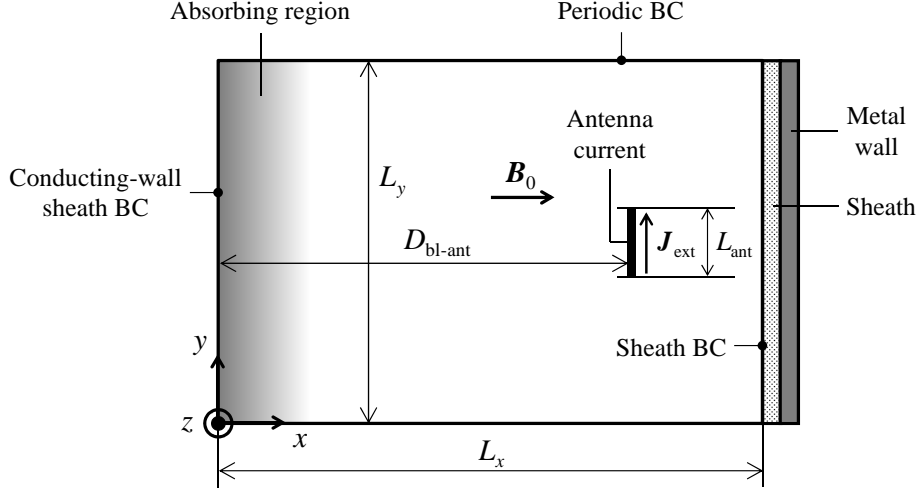


Figure 5: Singly periodic slab model for the analysis of RF sheath-plasma interactions.

Fig. 6 shows the filled contour plot of $\text{Im}(E_{\parallel})/K_{\max}$ for $k_z = 320 \text{ m}^{-1}$ at $K_{\max} = 10 \text{ A/m}$, where E_{\parallel} is the component of \mathbf{E} parallel to the background magnetic field \mathbf{B}_0 (i.e., $E_{\parallel} = \mathbf{E} \cdot \mathbf{b} = E_x$). Here, the antenna and magnetic field lines are also superimposed on the plot. The result is obtained by imposing the generalized sheath BC on the sheath surface at $x = L_x$. It is observed that the slow wave (SW) propagates along the magnetic field lines, since this is a plot showing E_{\parallel} in which the fast wave contribution is considered to be negligible. In order to verify the accuracy of the wavelength in the x direction, one can employ the cold plasma dispersion relation which includes n_{\parallel} (the component of the index of refraction parallel to \mathbf{B}_0) and n_{\perp} (the component of the index of refraction perpendicular to \mathbf{B}_0) [29]. Since the present case (for $k_z = 320 \text{ m}^{-1}$) satisfies $|n_{\perp}^2| \simeq |ck_z/\omega|^2 \gg |\varepsilon_{\parallel}|$ and $|\varepsilon_{\parallel}| \gg |\varepsilon_{\perp}|$, the dispersion relation is approximately given by

$$n_{\parallel}^4 \varepsilon_{\parallel} + n_{\parallel}^2 n_{\perp}^2 \varepsilon_{\parallel} + n_{\perp}^4 \varepsilon_{\perp} = 0. \quad (29)$$

A further approximate expression for the small n_{\parallel} root is obtained by balancing the last two terms in Eq. (29):

$$n_{\parallel}^2 \varepsilon_{\parallel} + n_{\perp}^2 \varepsilon_{\perp} = 0, \quad (30)$$

which is recognized as the electrostatic limit of the SW dispersion relation. Then, the SW root is approximately $n_{\parallel} = \pm 4.3$ or $k_{\parallel} = \mathbf{k} \cdot \mathbf{b} = \pm 7.2 \text{ m}^{-1}$

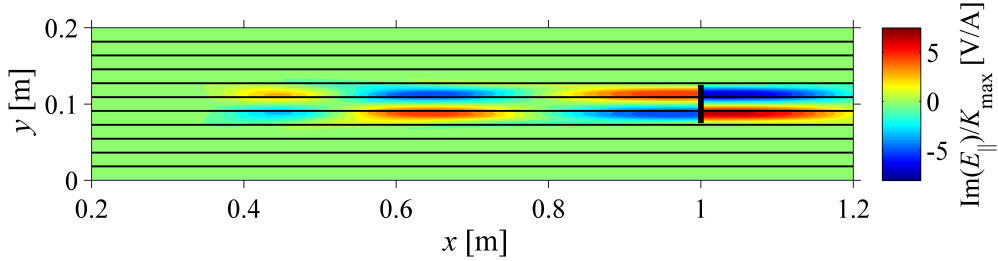


Figure 6: Filled contour plot of $\text{Im}(E_{\parallel})/K_{\max}$ for $n_0 = 1 \times 10^{17} \text{ m}^{-3}$ and $k_z = 320 \text{ m}^{-1}$ at $K_{\max} = 10 \text{ A/m}$, which is obtained by imposing the generalized sheath BC on the sheath surface.

(neglecting the contribution of k_y to k_{\perp}). This gives a half wavelength of 0.44 m which is reasonably close to the estimated wavelength near the antenna in Fig. 6.

The profiles of $|V_{\text{RF}}|_{\max}$ as a function of K_{\max} are compared between the capacitive sheath model and the sheath impedance model for $k_z = 160 \text{ m}^{-1}$ and $k_z = 320 \text{ m}^{-1}$ in Fig. 7(a) and (b), respectively. Here, $|V_{\text{RF}}|_{\max}$ is the maximum absolute value of the RF sheath voltage on the sheath surface. It is seen in both plots that $|V_{\text{RF}}|_{\max}$ for the sheath impedance model is smaller than that for the capacitive sheath model at any value of K_{\max} because of the presence of the sheath power dissipation. (Therefore, the general sheath impedance model is expected to reduce RF sheath voltages relative to the capacitive sheath limit; an exception might occur if a resonance condition is present.) The almost linear variations partly observed in both plots are attributed to the fact that $|D_n|/K_{\max}$ decreases with the increase in Δ_{sh} for the capacitive sheath model [23] and $|z_{\text{sh}}|$ for the sheath impedance model (see Fig. 9 below) when the values of K_{\max} are sufficiently large. In such cases, the sheath is in a quasi-insulating limit.

It is also observed that the relative difference in $|V_{\text{RF}}|_{\max}$ between the two models is larger for $k_z = 160 \text{ m}^{-1}$ than for $k_z = 320 \text{ m}^{-1}$, especially at low voltages. The reason for this is explained as follows. In general, the value of the sheath impedance parameter z_{sh} relative to the wave impedance parameter z_w determines how strongly the sheath model affects the solution. In short, the solution is insensitive to the sheath model when $|z_{\text{sh}}/z_w| \gg 1$, whereas it becomes sensitive when $|z_{\text{sh}}/z_w| \sim 1$. At very high voltages, the sheath impedance parameter in either model gets very large for both $k_z = 160 \text{ m}^{-1}$ and $k_z = 320 \text{ m}^{-1}$, and the quasi-insulating limit applies as described

above; in such a case, we obtain $|z_{\text{sh}}/z_{\text{w}}| \gg 1$. On the other hand, the sensitivity occurs when the absolute value of the RF sheath voltage is small at low k_z , which yields $|z_{\text{sh}}| \sim 1$ and $|z_{\text{w}}| \sim 1$. The dependence of z_{w} on k_z ($\sim k_{\perp}$) can be seen from the expression for z_{w} in the electrostatic limit, which is given by $1/z_{\text{w}} = J_{\parallel}/\Phi = \omega\varepsilon_0 k_{\perp} (\varepsilon_{\perp}\varepsilon_{\parallel})^{1/2}$.

The plot of the maximum power per unit area on the sheath, P_{max} , as a function of K_{max} for $k_z = 320 \text{ m}^{-1}$ is shown in Fig. 8. (Hereafter, the power per unit area on the sheath is simply called the power density.) The power density (denoted by P) used here is defined as

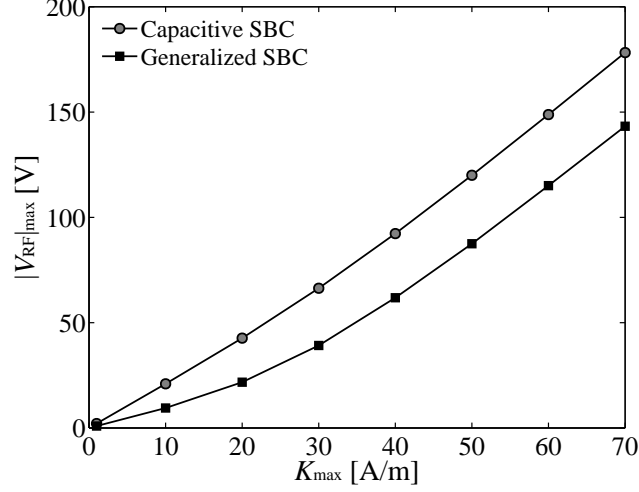
$$P \equiv \frac{1}{2} |J_x^{(\text{sh})}|^2 \text{Re}(z_{\text{sh}}) = \frac{\omega^2}{2} |D_x^{(\text{pl})}|^2 \text{Re}(z_{\text{sh}}) \Big|_{x=L_x} \quad (31)$$

(see Appendix C for the derivation of this expression). Note that nonzero power density is obtained only by employing the generalized sheath BC, since $\text{Re}(z_{\text{sh}}) = 0 \text{ } \Omega\text{m}^2$ for the capacitive sheath BC. It is seen that P_{max} increases in proportion to K_{max} for $K_{\text{max}} > 30 \text{ A/m}$. For this low-density plasma (associated with a propagating SW), the maximum power density is so low that material damage should not occur even when the absolute value of the RF sheath voltage is close to 150 V.

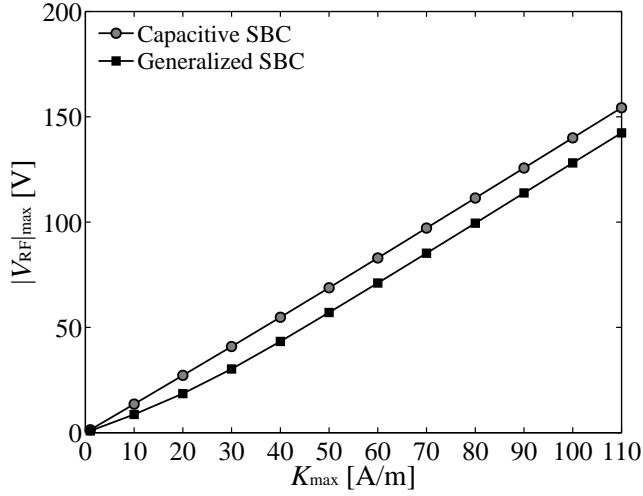
Fig. 9 shows the plot of the maximum real and imaginary parts of \hat{z}_{sh} on the sheath, $\text{Re}(\hat{z}_{\text{sh}})_{\text{max}}$ and $\text{Im}(\hat{z}_{\text{sh}})_{\text{max}}$, as functions of K_{max} for $k_z = 320 \text{ m}^{-1}$ under the generalized sheath BC. As shown in this plot, the magnitude relation of the real and imaginary parts changes between $K_{\text{max}} = 40 \text{ A/m}$ and $K_{\text{max}} = 50 \text{ A/m}$. This is consistent with expectations based on recent analytical analysis [26] of the form of the electron and displacement current admittance parameters (denoted by \hat{y}_e and \hat{y}_d in dimensionless form, respectively) for high voltages: $\hat{y}_e \sim |V_{\text{RF}}|^{-1}$ and $\hat{y}_d \sim |V_{\text{RF}}|^{-3/4}$ (see also Appendix A), so that for large enough $|V_{\text{RF}}|$, \hat{y}_d will dominate. Note that the contribution of ions to the (total) sheath admittance parameter is negligibly small over the entire range of K_{max} considered in this case.

5.2. Interactions with evanescent waves in a high-density plasma

Second, we consider cases where a high-density plasma fills in the 2D slab domain. The high density case is of particular concern because of the possibility of greater surface power dissipation, as we shall see. For sufficiently high densities, the SW is evanescent, which may help to alleviate interactions if the source of the waves is sufficiently removed from the material surfaces.



(a)



(b)

Figure 7: Comparison of the profiles of $|V_{\text{RF}}|_{\max}$ (maximum absolute value of the RF sheath voltage on the sheath surface) as a function of K_{\max} between the capacitive sheath model (employing the capacitive sheath BC) and the sheath impedance model (employing the generalized sheath BC) for $k_z = 160 \text{ m}^{-1}$ (a) and $k_z = 320 \text{ m}^{-1}$ (b). Here, the plasma density n_0 is $1 \times 10^{17} \text{ m}^{-3}$.

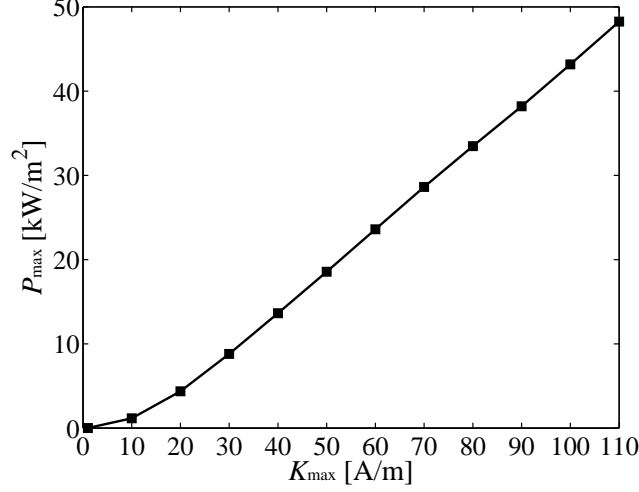


Figure 8: Plot of P_{\max} (maximum power per unit area on the sheath) vs. K_{\max} for $n_0 = 1 \times 10^{17} \text{ m}^{-3}$ and $k_z = 320 \text{ m}^{-1}$, which is obtained by imposing the generalized sheath BC on the sheath surface.

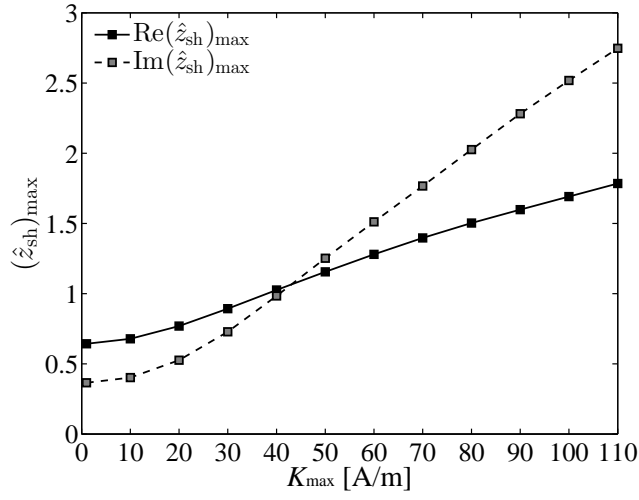


Figure 9: Plot of $\text{Re}(\hat{z}_{\text{sh}})_{\max}$ and $-\text{Im}(\hat{z}_{\text{sh}})_{\max}$ (maximum values of the real and imaginary parts of the dimensionless sheath impedance parameter) vs. K_{\max} for $n_0 = 1 \times 10^{17} \text{ m}^{-3}$ and $k_z = 320 \text{ m}^{-1}$, which is obtained by imposing the generalized sheath BC on the sheath surface.

Several studies using full wave codes have investigated evanescent SWs near bounding surfaces [5, 15, 18] motivated in part by the importance of controlling large parallel electric fields near the antenna [7, 10, 17]. In Ref. [5], a model geometry was employed to illustrate the formation of boundary sheaths from an evanescent SW, and its dependence on the SW evanescence length. This study employed the capacitive sheath BC, retaining a self-consistent sheath width model similar to Eq. (25). Studies were carried out in Ref. [18] using a more realistic model of the antenna fields, invoking the capacitive sheath BC but in a wide sheath quasi-insulating limit. Here, we consider the evanescent SW case using the generalized sheath BC and compare results with the capacitive BC case.

In this subsection, the plasma density n_0 is fixed at $2 \times 10^{18} \text{ m}^{-3}$, and the calculations are again carried out with two different values of k_z : 160 m^{-1} and 320 m^{-1} . The absorbing layer is not necessary in these cases, because the waves from the antenna are evanescent (as will be described below).

Fig. 10 shows the filled contour plot of $\text{Im}(E_{\parallel})/K_{\text{max}}$ for $k_z = 320 \text{ m}^{-1}$ at $K_{\text{max}} = 200 \text{ A/m}$. This is obtained by imposing the generalized sheath BC on the sheath surface at $x = L_x$. It is observed that the SW is evanescent along the magnetic field lines. In order to verify the accuracy of the evanescence length in the x direction, the approximate dispersion relation (29) (and hence the electrostatic limit (30)) should not be employed, since the condition $|n_{\perp}^2| \gg |\varepsilon_{\parallel}|$ is not well satisfied. Instead, the full electromagnetic SW dispersion relation generalizes Eq. (30) to

$$n_{\parallel}^2 \varepsilon_{\parallel} + n_{\perp}^2 \varepsilon_{\perp} = \varepsilon_{\perp} \varepsilon_{\parallel}. \quad (32)$$

For the case shown in Fig. 10, this gives $n_{\parallel} = \pm 3.8i$ or an e-folding length $|k_{\parallel}|^{-1} = 0.16 \text{ m}$ in good agreement with the figure.

The profiles of $|V_{\text{RF}}|_{\text{max}}$ as a function of K_{max} are compared between the capacitive sheath model and the sheath impedance model for $k_z = 160 \text{ m}^{-1}$ and $k_z = 320 \text{ m}^{-1}$ in Fig. 11(a) and (b), respectively. The results are qualitatively similar to those shown in Fig. 7(a) and (b); for these high density cases, we have $\omega/\omega_{\text{pi}} = 0.38$ and this ratio is far from the capacitive limit $\omega/\omega_{\text{pi}} \gg 1$ [25], which can be the cause of the large difference in voltage values between the sheath models for $k_z = 160 \text{ m}^{-1}$ (in comparison with the difference for $k_z = 160 \text{ m}^{-1}$ in the low density case). However, compared to the results shown in Fig. 7, we see that much higher antenna current density (on the order of a few kA/m) is required to yield $|V_{\text{RF}}|_{\text{max}} > 100 \text{ V}$ for the

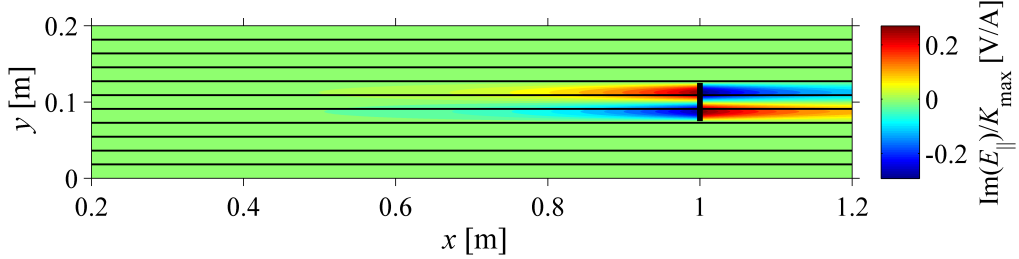


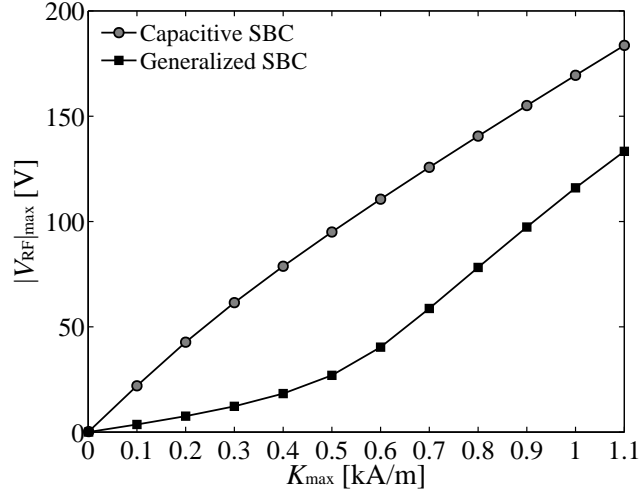
Figure 10: Filled contour plot of $\text{Im}(E_{\parallel})/K_{\max}$ for $n_0 = 2 \times 10^{18} \text{ m}^{-3}$ and $k_z = 320 \text{ m}^{-1}$ at $K_{\max} = 200 \text{ A/m}$, which is obtained by imposing the generalized sheath BC on the sheath surface.

present cases. On the other hand, it turns out that the maximum absolute values of E_{\parallel} around $|V_{\text{RF}}|_{\max} = 150 \text{ V}$ are of the same order in both density cases. For example, with the use of the generalized sheath BC, we obtain $|E_{\parallel}|_{\max} = 222 \text{ V/m}$ corresponding to $|V_{\text{RF}}|_{\max} = 142 \text{ V}$ at $K_{\max} = 110 \text{ A/m}$ in Fig. 7(b) and $|E_{\parallel}|_{\max} = 153 \text{ V/m}$ corresponding to $|V_{\text{RF}}|_{\max} = 149 \text{ V}$ at $K_{\max} = 3.6 \text{ kA/m}$ in Fig. 11(b). The reason for this is related to the difference in characteristics of waves; as described above, the SW is propagating in the low-density plasma, while the SW is evanescent in the high-density plasma. Substituting Eq. (23) into the top right-hand side of Eq. (4) and noting that $D_n = -\varepsilon_0 \varepsilon_{xx} E_x \simeq \varepsilon_0 \omega_{\text{pe}}^2 E_x / \omega^2$ (where ω_{pe} is the electron plasma frequency), we obtain the following relation between V_{RF} and E_x :

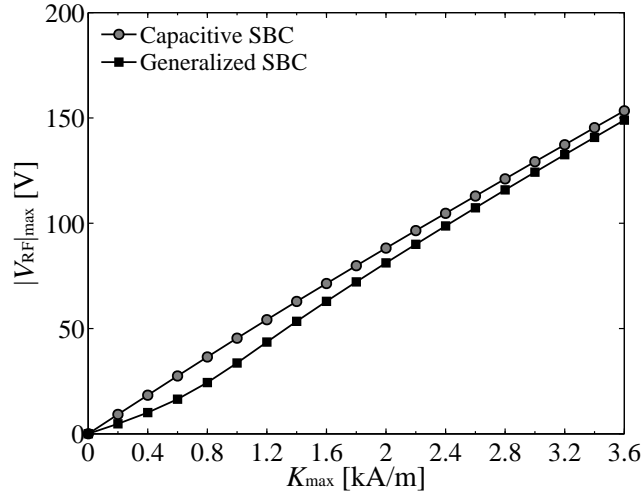
$$V_{\text{RF}} = i \frac{m_i c_s}{m_e \omega} \hat{z}_{\text{sh}} E_x, \quad (33)$$

where $c_s = (T_e/m_i)^{1/2}$ and m_e is the electron mass. It can be seen from Eq. (33) that the plasma density on the sheath surface does not explicitly appear in the expression for V_{RF} (although \hat{z}_{sh} depends on the plasma density). Since V_{RF} and E_x are similar in the two cases, the maximum absolute values of \hat{z}_{sh} around $|V_{\text{RF}}|_{\max} = 150 \text{ V}$ should also be of the same order in both density cases. In fact, with the use of the generalized sheath BC, we obtain $|\hat{z}_{\text{sh}}|_{\max} = 3.28$ at $K_{\max} = 110 \text{ A/m}$ in Fig. 7(b) and $|\hat{z}_{\text{sh}}|_{\max} = 4.97$ at $K_{\max} = 3.6 \text{ kA/m}$ in Fig. 11(b) (see Figs. 9 and 13). This explains the fact that the high density case has a higher current but a similar sheath voltage compared with the low density case. It also suggests that the sheath power dissipation will be larger in the high density case. We consider this next.

The plot of P_{\max} as a function of K_{\max} for $k_z = 320 \text{ m}^{-1}$ is shown in



(a)



(b)

Figure 11: Comparison of the profiles of $|V_{\text{RF}}|_{\text{max}}$ as a function of K_{max} between the capacitive sheath model and the sheath impedance model for $k_z = 160 \text{ m}^{-1}$ (a) and $k_z = 320 \text{ m}^{-1}$ (b). Here, the plasma density n_0 is $2 \times 10^{18} \text{ m}^{-3}$.

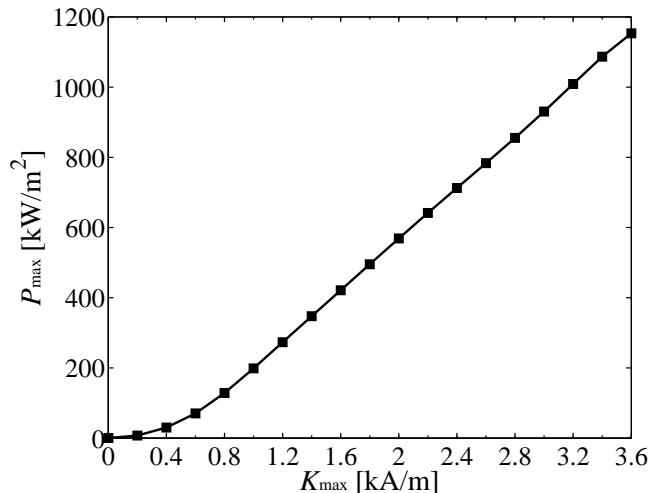


Figure 12: Plot of P_{\max} vs. K_{\max} for $n_0 = 2 \times 10^{18} \text{ m}^{-3}$ and $k_z = 320 \text{ m}^{-1}$, which is obtained by imposing the generalized sheath BC on the sheath surface.

Fig. 12. We see that an almost linear profile similar to the result shown in Fig. 8 is obtained, but P_{\max} corresponding to $|V_{\text{RF}}|_{\max} \simeq 150 \text{ V}$ for the high density case is approximately 20 times greater than that for the lower density case. This difference is understood by noting that $P \sim V_{\text{RF}} J_n$; we have shown that V_{RF} is nearly independent of the plasma density, while $J_n \sim \omega D_n \propto \epsilon_{xx} \propto n_0$. Then, it can be concluded that the difference in the maximum power density is mostly consistent with the difference in the plasma density. A power density on the order of a few MW/m² is likely to cause irreversible damage unless the wall material is carefully selected.

Fig. 13 shows the plot of $\text{Re}(\hat{z}_{\text{sh}})_{\max}$ and $\text{Im}(\hat{z}_{\text{sh}})_{\max}$ as functions of K_{\max} for $k_z = 320 \text{ m}^{-1}$ under the generalized sheath BC. Unlike the plot shown in Fig. 9, the relative magnitudes of the real and imaginary parts do not change over the entire range of K_{\max} . At high density, where ω_{pi} is large, $\hat{\omega} = \omega/\omega_{\text{pi}}$ is small and the dimensionless displacement current admittance parameter \hat{y}_d is reduced since $\hat{y}_d = -i\hat{\omega}/\hat{\Delta}_{\text{sh}}$ (see Eq. (A.9) in Appendix A). On the other hand, the dimensionless electron admittance parameter \hat{y}_e is purely real and insensitive to $\hat{\omega}$. Since $\hat{z}_{\text{sh}} \simeq (\hat{y}_e + \hat{y}_d)^{-1}$, the higher density result in Fig. 13 exhibits a larger $\text{Re}(\hat{z}_{\text{sh}})_{\max}$ and a smaller $\text{Im}(\hat{z}_{\text{sh}})_{\max}$ relative to the lower density result in Fig. 9.

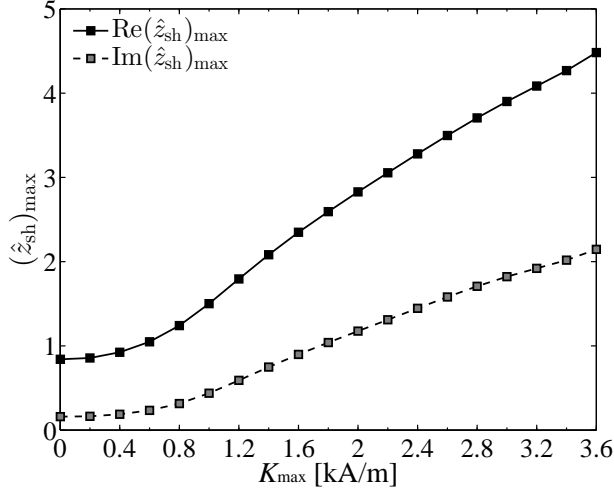
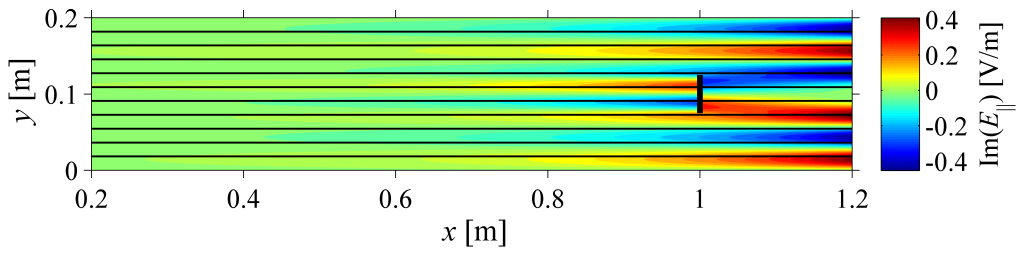


Figure 13: Plot of $\text{Re}(\hat{z}_{\text{sh}})_{\max}$ and $\text{Im}(\hat{z}_{\text{sh}})_{\max}$ vs. K_{\max} for $n_0 = 2 \times 10^{18} \text{ m}^{-3}$ and $k_z = 320 \text{ m}^{-1}$, which is obtained by imposing the generalized sheath BC on the sheath surface.

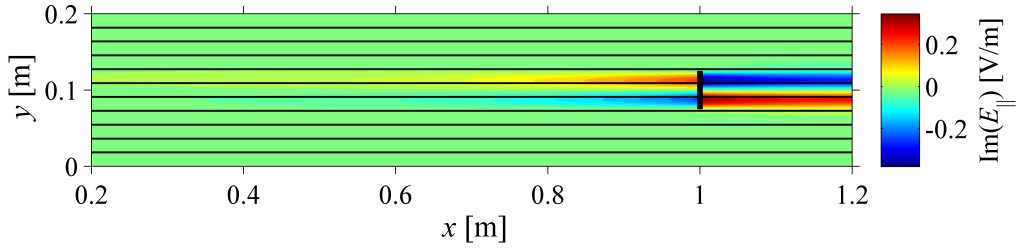
5.3. Suppression of the sheath-plasma wave resonance

Lastly, we consider cases where a high-density plasma fills in the 2D slab domain and relatively small values of k_z are prescribed. Here, the plasma density n_0 and antenna current density K_{\max} are fixed at $2 \times 10^{18} \text{ m}^{-3}$ and 1 A/m, respectively, and the calculations are carried out with the values of k_z in the range of 50 to 120 m^{-1} . The absorbing layer is not necessary, because the waves from the antenna are evanescent as described in Section 5.2.

Fig. 14(a) and (b) show the filled contour plots of $\text{Im}(E_{\parallel})$ at $k_z = 50 \text{ m}^{-1}$, which are obtained using the capacitive sheath BC and the generalized sheath BC, respectively. It is seen in Fig. 14(a) that the SPW propagates along the sheath surface, whereas it is not observed in Fig. 14(b). Here, we select a case with very small K_{\max} and small $\hat{\omega}$ (i.e., $\hat{\omega} = 0.38 < 1$) to illustrate that the effect of the generalized sheath BC on the SPW can be dramatic for some parameters. For this case, the dimensionless sheath impedance parameters, which are nearly constant along the sheath surface, are $\text{Re}(\hat{z}_{\text{sh}}) = 0$ and $\text{Im}(\hat{z}_{\text{sh}}) = 7.6$ for the capacitive sheath model (see Eq. (22)) and $\text{Re}(\hat{z}_{\text{sh}}) = 0.84$ and $\text{Im}(\hat{z}_{\text{sh}}) = 0.16$ for the sheath impedance model. The combined effect of the significant change of $|\hat{z}_{\text{sh}}|$ together with the sheath power dissipation through nonzero $\text{Re}(\hat{z}_{\text{sh}})$ completely eliminates the SPW under the generalized sheath BC.



(a)



(b)

Figure 14: Comparison of the filled contour plots of $\text{Im}(E_{\parallel})$ for $n_0 = 2 \times 10^{18} \text{ m}^{-3}$ and $K_{\text{max}} = 1 \text{ A/m}$ at $k_z = 50 \text{ m}^{-1}$, which are obtained using the capacitive sheath BC (a) and the generalized sheath BC (b).

The profiles of $|V_{\text{RF}}|_{\text{max}}$ as a function of k_z are compared between the capacitive sheath model and the sheath impedance model in Fig. 15. It can be seen that the SPW resonances appear at some particular values of k_z when the capacitive sheath BC is used. On the other hand, no resonance appears with the generalized sheath BC imposed on the sheath surface; the maximum sheath voltages are much lower than those obtained under the capacitive sheath BC and vary almost linearly from 4.44×10^{-2} V at $k_z = 50$ m^{-1} to 3.87×10^{-2} V at $k_z = 120$ m^{-1} . (Recall that the antenna current density is very small in this example.) When the resonance occurs on the sheath surface, the y component of the wave vector of the SPW, $k_{\text{SPW},y}$, is given by $k_{\text{SPW},y} = 2\pi m/L_y$, where m is the mode number. In Fig. 15, we see that the SPW resonances at $m = 1, 2,$ and 3 occur when the values of k_z are 115.6, 102, and 74 m^{-1} , respectively. These numerical results reasonably agree with the analytical solution, as shown in Fig. 16; here, the sheath width Δ_{sh} is fixed at 5.87×10^{-5} m (corresponding to the Bohm sheath contribution, i.e., $\Delta_{\text{sh}} = \left\{ \ln \left[(m_i/m_e)^{1/2} \right] \right\}^{3/4} \lambda_{\text{De}}$) in the analytical solution. (The analytical expressions for the wave vector components of the SPW based on electromagnetic theory are derived in Appendix D.) The mismatch between the analytical solution and the numerically obtained resonance conditions in Fig. 16 may be attributed to the fact that the analytical solution curve is obtained using the second-order SW approximation instead of the full quartic equation (for n_{\parallel} or n_{\perp}) for the SPW.

6. Conclusions

In this paper, we presented a new numerical scheme for analyzing self-consistent RF sheath-plasma interactions in RF plasma heating used to achieve nuclear fusion in tokamak devices. In a similar way to the previous approach using the capacitive sheath BC [23], a combined form of Maxwell's equations and the generalized form of the sheath BC are both discretized by finite element methods, and the obtained discretized equations are combined into a vector equation. In addition, the relation between the RF voltage across the sheath and the total current density (including the particle and displacement current densities) in the sheath is incorporated into the vector equation to additionally obtain the local RF sheath voltage as part of the numerical solution. The sheath impedance parameter used in this relation has both capacitance and resistance contributions and is characterized by

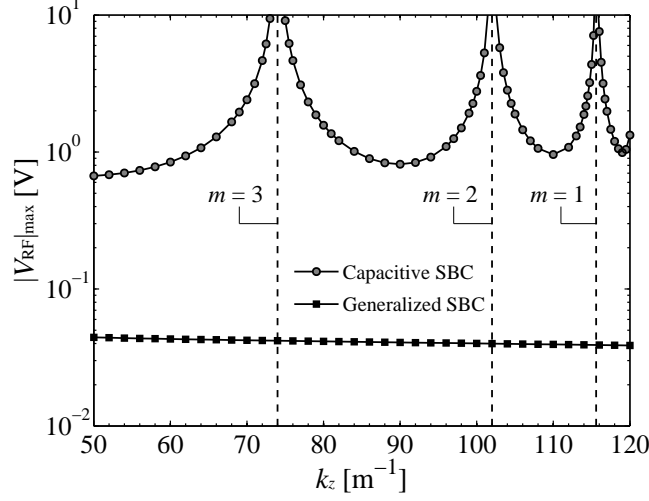


Figure 15: Comparison of the profiles of $|V_{\text{RF}}|_{\text{max}}$ as a function of k_z between the capacitive sheath model and the sheath impedance model for $n_0 = 2 \times 10^{18} \text{ m}^{-3}$ and $K_{\text{max}} = 1 \text{ A/m}$. The vertical dashed lines indicate the values of k_z corresponding to the resonances at $m = 1, 2,$ and 3 .

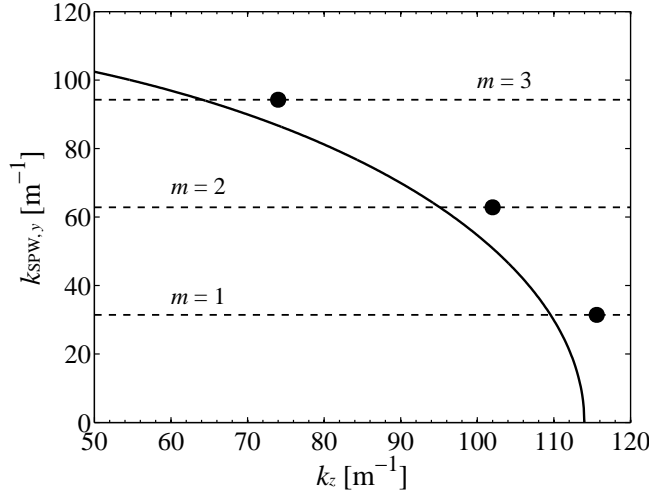


Figure 16: Plot of $k_{\text{SPW},y}$ vs. k_z for $n_0 = 2 \times 10^{18} \text{ m}^{-3}$ and $K_{\text{max}} = 1 \text{ A/m}$: the solid curve denotes the analytical solution (obtained from Eqs. (D.6) and (D.7) in Appendix D with the use of $\Delta_{\text{sh}} = 5.87 \times 10^{-5} \text{ m}$) and the solid circles denote the resonance conditions obtained using the code for the capacitive sheath (see Fig. 15). The horizontal dashed lines indicate the values of $k_{\text{SPW},y}$ corresponding to the resonances at $m = 1, 2,$ and 3 .

four dimensionless input parameters in general [25].

In Sections 4 and 5, we have solved some sheath-plasma interaction problems with the direction of the background magnetic field perpendicular to the sheath surface(s). This simplified condition reduces the dimensionality of the sheath impedance parameter in such a way that it can be expressed as a function of two independent variables. The validity of the developed code (new rfSOL code) was confirmed through a comparison with an analytical solution in the 1D closed domain filled by a uniform plasma. It was also demonstrated that the proposed scheme does not reduce to the previous finite element scheme even in the capacitive sheath limit due to the difference in the expression for the rectified sheath voltage; note that the present version is based on an improved physics model. In the numerical analysis using the 2D slab domain filled by low- and high-density plasmas, it was found that the difference in the maximum absolute value of the RF sheath voltage between the capacitive sheath model and the sheath impedance model is large when the sheath voltage is not extremely large at a lower wave vector component (specified in the direction perpendicular to the antenna current and parallel to the sheath surface) and a high-density plasma (see Fig. 11(a)). Because the generalized sheath impedance model contains a resistive contribution, we have been able to demonstrate for the first time a self-consistent full wave calculation that includes the sheath power dissipation. It was shown that for high-voltage sheaths (~ 100 V) in a high-density plasma, the maximum power per unit area on the sheath can be on the order of a few MW/m², which may be enough to cause damage to material surfaces in fusion devices. Furthermore, it was demonstrated that the presence of the sheath resistance can suppress the sheath-plasma wave resonances, which occur in the capacitive sheath limit, under certain conditions.

The next step will be improvement of the expression for the sheath impedance parameter so as to deal with cases where the background magnetic field makes an oblique angle with the sheath surface. It should be emphasized that the finite element scheme presented in this study can be straightforwardly applied to such general cases as long as the sheath impedance parameter is smooth with respect to four dimensionless input parameters.

Acknowledgments

Discussions with the rf-SciDAC team (Center for Simulation of Wave-Plasma Interactions) are gratefully acknowledged. This material is based

upon work supported by JSPS KAKENHI Grant Number JP16K18336 and the U.S. Department of Energy Office of Science, Office of Fusion Energy Sciences, under Award No. DE-FC02-05ER54823. This research used resources of the National Energy Research Scientific Computing Center, a DOE Office of Science User Facility supported by the Office of Science of the U.S. Department of Energy under Contract No. DE-AC02-05CH11231. Digital data for the figures presented in this paper may be found in Supplementary Material.

Appendix A. An explicit expression for the dimensionless sheath admittance parameter

In this appendix, we explicitly show the approximate analytical forms to express the dimensionless sheath admittance parameter \hat{y}_{sh} for a background magnetic field perpendicularly intersected with the sheath surface, which are used in the numerical examples in Sections 4 and 5. Although in general \hat{y}_{sh} is a function of $\hat{\Omega}$, b_n , $\hat{\omega}$, and \tilde{V}_{RF} (see Section 2), this simplest case reduces the dimensionality to $\hat{y}_{\text{sh}}(\hat{\omega}, \tilde{V}_{\text{RF}})$. All of the fits provided in this appendix only apply over the range $0 < \hat{\omega} < 8$ and $0 < \tilde{V}_{\text{pp}} < 20$, where \tilde{V}_{pp} is the dimensionless peak-to-peak voltage which is related to \tilde{V}_{RF} by $\tilde{V}_{\text{pp}} = 2\tilde{V}_{\text{RF}}$.

The fits given in this appendix were obtained from a series of computations using the numerical model presented in Ref. [25]. A total of 210 runs covering the parameter space of $\hat{\omega}$ and \tilde{V}_{pp} in the indicated ranges were carried out and fit to polynomial expressions using the forms indicated in the following. The physics basis for a better parameterization, making use of asymptotic analytical results and rational functions allowing infinite domains in the parameters, is described in Ref. [26]. More details of these fits will be provided elsewhere.

The dimensionless sheath admittance parameter is written as

$$\hat{y}_{\text{sh}} = \hat{y}_i + \hat{y}_e + \hat{y}_d, \quad (\text{A.1})$$

including the contributions of ions, electrons, and displacement current. First, the dimensionless ion admittance parameter \hat{y}_i is found to be well described by scaling the frequency dependence at an intermediate value of voltage, $\tilde{V}_{\text{pp}} = 10$, as follows:

$$\hat{y}_i(\hat{\omega}, \tilde{V}_{\text{pp}}) \equiv \frac{\mathcal{F}_2(\tilde{V}_{\text{pp}})}{\mathcal{F}_2(10)} \hat{y}'_i \left(\hat{\omega} \frac{\mathcal{F}_1(10)}{\mathcal{F}_1(\tilde{V}_{\text{pp}})} \right), \quad (\text{A.2})$$

where

$$\mathcal{F}_1(\chi) \equiv 1.0042 - 4.0348 \times 10^{-2}\chi + 1.5929 \times 10^{-3}\chi^2 - 2.8424 \times 10^{-5}\chi^3 + 6.4358 \times 10^{-2} \tanh(0.5\chi), \quad (\text{A.3})$$

$$\mathcal{F}_2(\chi) \equiv 0.10853 - 6.2442 \times 10^{-3}\chi + 2.4235 \times 10^{-4}\chi^2 - 4.1991 \times 10^{-6}\chi^3 + 8.9064 \times 10^{-3} \tanh(0.5\chi), \quad (\text{A.4})$$

$$\hat{y}'_i(\chi) \equiv \mathcal{G}_1(\chi) e^{i\mathcal{G}_2(\chi)}, \quad (\text{A.5})$$

$$\begin{aligned} \mathcal{G}_1(\chi) \equiv & 1.3542 \times 10^{-4} - 5.2148 \times 10^{-2}\chi + 0.28344\chi e^{-\chi} \\ & + 3.0533 \times 10^{-2}\chi^2 - 6.4774 \times 10^{-3}\chi^3 \\ & + 6.0997 \times 10^{-4}\chi^4 - 2.1658 \times 10^{-5}\chi^5, \end{aligned} \quad (\text{A.6})$$

$$\begin{aligned} \mathcal{G}_2(\chi) \equiv & -1.5283 + 0.72924\chi - 0.17952\chi^2 \\ & + 1.9827 \times 10^{-2}\chi^3 - 8.1711 \times 10^{-4}\chi^4 \\ & + 1.8339 \tanh(0.91\chi). \end{aligned} \quad (\text{A.7})$$

Second, the dimensionless electron admittance parameter \hat{y}_e is

$$\begin{aligned} \hat{y}_e(\tilde{V}_{\text{pp}}) \equiv & 1.4913 - 0.39149e^{-\tilde{V}_{\text{pp}}} - 0.35029\tilde{V}_{\text{pp}} \\ & + 4.3703 \times 10^{-2}\tilde{V}_{\text{pp}}^2 - 2.9807 \times 10^{-3}\tilde{V}_{\text{pp}}^3 \\ & + 1.0448 \times 10^{-4}\tilde{V}_{\text{pp}}^4 - 1.4687 \times 10^{-6}\tilde{V}_{\text{pp}}^5. \end{aligned} \quad (\text{A.8})$$

Lastly, the dimensionless displacement current admittance parameter \hat{y}_d is given by

$$\hat{y}_d(\hat{\omega}, \tilde{V}_{\text{pp}}) \equiv -i \frac{\hat{\omega}}{\hat{V}_{\text{rect}}(\tilde{V}_{\text{pp}})^{3/4}}, \quad (\text{A.9})$$

where

$$\begin{aligned} \hat{V}_{\text{rect}}(\chi) \equiv & 3.0670 + 6.2485 \times 10^{-2}\chi + 4.6812 \times 10^{-2}\chi^2 \\ & - 2.4363 \times 10^{-3}\chi^3 + 4.6927 \times 10^{-5}\chi^4. \end{aligned} \quad (\text{A.10})$$

It is important to note that these expressions are differentiable in the real and imaginary parts of the RF sheath voltage V_{RF} . This is required in the rfSOL code because the derivatives of z_{sh} with respect to $\text{Re}(\hat{V}_{\text{RF}})$ and

$\text{Im}(\hat{V}_{\text{RF}})$ at each node on the sheath surface need to be computed in the present Newton–Raphson method (see Appendix B). At node i' on the sheath surface, the dimensional sheath impedance parameter $z_{\text{sh},i'}$ is obtained from the dimensionless sheath admittance parameter $\hat{y}_{\text{sh},i'}$ and some dimensional quantities at the node (denoted by the subscript i') as follows:

$$z_{\text{sh},i'} = \frac{\lambda_{\text{De},i'}}{\varepsilon_0 \omega_{\text{pi},i'}} \hat{y}_{\text{sh},i'}^{-1} = \frac{\lambda_{\text{De},i'}}{\varepsilon_0 \omega_{\text{pi},i'}} \hat{z}_{\text{sh},i'}. \quad (\text{A.11})$$

The inaccuracy in the present fits is about 10 % in the worst cases; however, it is much better over most of the range of interest. As mentioned in the beginning, the parameterization of the sheath admittance parameter will be further improved in the future in order to achieve better accuracy and remove the necessity to set upper limits of $\hat{\omega}$ and \hat{V}_{pp} .

Appendix B. Newton–Raphson method

The present finite element equations and the equations to satisfy the current-voltage relation in the sheath are put together and expressed as

$$\mathbf{L} = \mathbf{R}, \quad (\text{B.1})$$

where

$$\begin{aligned} \mathbf{L} = & \left(F_{x(1)}^{(\text{R})}, \dots, F_{x(\text{NP})}^{(\text{R})}, F_{y(1)}^{(\text{R})}, \dots, F_{y(\text{NP})}^{(\text{R})}, F_{z(1)}^{(\text{R})}, \dots, F_{z(\text{NP})}^{(\text{R})}, \right. \\ & F_{v(1)}^{(\text{R})}, \dots, F_{v(\text{NB})}^{(\text{R})}, G_{\tau(1)}^{(\text{R})}, \dots, G_{\tau(\text{NB})}^{(\text{R})}, G_{z(1)}^{(\text{R})}, \dots, G_{z(\text{NB})}^{(\text{R})}, \\ & F_{x(1)}^{(\text{I})}, \dots, F_{x(\text{NP})}^{(\text{I})}, F_{y(1)}^{(\text{I})}, \dots, F_{y(\text{NP})}^{(\text{I})}, F_{z(1)}^{(\text{I})}, \dots, F_{z(\text{NP})}^{(\text{I})}, \\ & F_{v(1)}^{(\text{I})}, \dots, F_{v(\text{NB})}^{(\text{I})}, G_{\tau(1)}^{(\text{I})}, \dots, G_{\tau(\text{NB})}^{(\text{I})}, G_{z(1)}^{(\text{I})}, \dots, G_{z(\text{NB})}^{(\text{I})}, \\ & \left. H_{(1)}^{(\text{R})}, \dots, H_{(\text{NS})}^{(\text{R})}, H_{(1)}^{(\text{I})}, \dots, H_{(\text{NS})}^{(\text{I})} \right), \end{aligned} \quad (\text{B.2})$$

$$\begin{aligned} \mathbf{R} = & \left(R_{x(1)}^{(\text{R})}, \dots, R_{x(\text{NP})}^{(\text{R})}, R_{y(1)}^{(\text{R})}, \dots, R_{y(\text{NP})}^{(\text{R})}, R_{z(1)}^{(\text{R})}, \dots, R_{z(\text{NP})}^{(\text{R})}, \right. \\ & 0, \dots, 0, 0, \dots, 0, 0, \dots, 0, \\ & R_{x(1)}^{(\text{I})}, \dots, R_{x(\text{NP})}^{(\text{I})}, R_{y(1)}^{(\text{I})}, \dots, R_{y(\text{NP})}^{(\text{I})}, R_{z(1)}^{(\text{I})}, \dots, R_{z(\text{NP})}^{(\text{I})}, \\ & 0, \dots, 0, 0, \dots, 0, 0, \dots, 0, \\ & \left. 0, \dots, 0, 0, \dots, 0 \right). \end{aligned} \quad (\text{B.3})$$

Here, F_x , F_y , and F_z are the x , y , and z components of \mathbf{F} , which corresponds to the discretized expression of Eq. (1) excluding the external current term, respectively, and F_v is the component of \mathbf{F} normal to the boundary; similarly, R_x , R_y , and R_z are the x , y , and z components of \mathbf{R} , which corresponds to the discretized expression of the external current term in Eq. (1), respectively (see Ref. [23]). (Note that, in fact, the real parts of R_x , R_y , and R_z are zero since \mathbf{J}_{ext} is a real vector.) Further, G_τ and G_z are the τ and z components of \mathbf{G} , which corresponds to the discretized expression of the sheath BC on the sheath surface (see Section 3) or \mathbf{E}_t for the conducting-wall BC on the core-edge plasma boundary; $H = 0$ is the current-voltage relation (again, see Section 3). The superscripts (R) and (I) denote real and imaginary parts, respectively; NP, NB, and NS in the subscripts are the total numbers of nodes in the plasma (excluding the boundaries), on the boundaries (including both the sheath surface and the core-edge plasma boundary), and on the sheath surface, respectively. (The total number of nodes on the core-edge plasma boundary is then NB – NS.) The numbers in the subscripts, each of which is shown with a parenthesis, are used as identification numbers for independent equations. The task here is to find the solution \mathbf{U} of the equation

$$\mathbf{f}(\mathbf{U}) = \mathbf{L} - \mathbf{R} = \mathbf{0} \quad (\text{B.4})$$

through the Newton–Raphson method. Here, \mathbf{U} is the real column vector which consists of the real and imaginary parts of $\hat{\mathbf{E}}_i$ and $\hat{V}_{\text{RF},i'}$, where $i = 1, \dots, \text{NP} + \text{NB}$ and $i' = 1, \dots, \text{NS}$. Note that the column vectors \mathbf{L} and \mathbf{R} cannot be replaced with the corresponding complex column vectors because the method requires the derivatives of $\hat{V}_{\text{RF},i'}$ ($= e|V_{\text{RF},i'}|/T_{e,i'}$) which are non-analytic in the complex variable sense.

Let us assume that an intermediate solution $\mathbf{U}^{(n)}$ is evaluated in the n -th iteration. Then, a set of linear equations for the correction $\delta\mathbf{U}^{(n)}$ is obtained by applying a Taylor series expansion to Eq. (B.4) and then neglecting high-order terms of the resultant equation, which is expressed as

$$\mathbf{K}^{(n)} \cdot \delta\mathbf{U}^{(n)} = -\mathbf{f}(\mathbf{U}^{(n)}), \quad (\text{B.5})$$

where

$$\mathbf{K}^{(n)} = (\nabla_{\mathbf{U}} \mathbf{f})^{\text{T}} \Big|_{\mathbf{U}^{(n)}}. \quad (\text{B.6})$$

Here, $\nabla_{\mathbf{U}}$ is the nabla operator with respect to \mathbf{U} in the abstract space of dimension $6(\text{NP} + \text{NB}) + 2\text{NS}$, and T is the transpose operation. Notice

that the expression of $\mathbf{K}^{(n)}$ is partly explicitly obtained using the discretized expressions of a combined form of Maxwell's equations (see Ref. [23]) and the sheath BC (see Eqs. (12) and (13)). The derivative expressions of the real and imaginary parts of the sheath impedance parameter z_{sh} with respect to the real and imaginary parts of \hat{V}_{RF} at each node on the sheath surface are approximately obtained by employing the symmetric difference quotient.

The intermediate solution is then improved by adding the correction:

$$\mathbf{U}^{(n+1)} = \mathbf{U}^{(n)} + \delta\mathbf{U}^{(n)}. \quad (\text{B.7})$$

The above process is iteratively conducted until the solution is fully converged. The present scheme adopts the following convergence criterion:

$$\left| \frac{\delta\hat{E}_{xi}^{(n)}}{\hat{E}_{xi}^{(n+1)}} \right|_{\max}, \left| \frac{\delta\hat{E}_{yi}^{(n)}}{\hat{E}_{yi}^{(n+1)}} \right|_{\max}, \left| \frac{\delta\hat{E}_{zi}^{(n)}}{\hat{E}_{zi}^{(n+1)}} \right|_{\max}, \left| \frac{\delta\hat{V}_{\text{RF},i'}^{(n)}}{\hat{V}_{\text{RF},i'}^{(n+1)}} \right|_{\max} < \varepsilon_{\text{err}} \quad (\text{B.8})$$

for $\left| \hat{E}_{xi}^{(n+1)} \right|, \left| \hat{E}_{yi}^{(n+1)} \right|, \left| \hat{E}_{zi}^{(n+1)} \right| > E_{\min}$ and $\left| \hat{V}_{\text{RF},i'}^{(n+1)} \right| > V_{\min}$. For the calculations in the 2D slab domains, the parameters ε_{err} , E_{\min} , and V_{\min} are fixed at 10^{-5} , 10^{-3} V/m, and 10^{-3} V, respectively.

Appendix C. Sheath power dissipation

In this appendix, we aim at rederiving the expressions for the sheath power dissipation (per unit length and per unit area) based on the 2D slab geometry of our model problem and comparing the calculated profiles of the power dissipation (per unit area) for code verification. An analytical demonstration using the relation between the power dissipation and the Poynting flux is also presented in Ref. [22].

First, the expression for the total power dissipated in the entire sheath region is given by

$$\mathcal{P}_{\text{tot}} \equiv \int_{\text{sheath}} \frac{1}{4} (\mathbf{J}^{(\text{sh})} \cdot \mathbf{E}^{(\text{sh})*} + \mathbf{J}^{(\text{sh})*} \cdot \mathbf{E}^{(\text{sh})}) dV, \quad (\text{C.1})$$

where the asterisk denotes complex conjugate. As described in Section 2, the electric field in the sheath is expressed by $\mathbf{E}^{(\text{sh})} = -\nabla\Phi_{\omega}^{(\text{sh})}$. Further, the approximation $\mathbf{J}^{(\text{sh})} \cdot \mathbf{E}^{(\text{sh})} \simeq J_n^{(\text{sh})} E_n^{(\text{sh})}$ is valid in the sheath region by noting that $|\mathbf{k}_t| \Delta_{\text{sh}} \ll 1$, where the subscripts n and t refer to the components

normal and tangential to the sheath surface, respectively. Then, Eq. (C.1) can be rewritten as

$$\mathcal{P}_{\text{tot}} \simeq -\frac{1}{4} \int_{\text{sheath}} \left(J_n^{(\text{sh})} \frac{\partial \Phi_\omega^{(\text{sh})*}}{\partial n} + J_n^{(\text{sh})*} \frac{\partial \Phi_\omega^{(\text{sh})}}{\partial n} \right) dV, \quad (\text{C.2})$$

where n denotes the normal coordinate defined at the sheath surface. Let us consider the sheath formed on one side of the 2D slab domain defined in Fig. 5. In the given coordinate system, the power per unit length in the z direction, $\hat{\mathcal{P}}_{\text{tot}}$, in the range $0 \leq y \leq L_y$ is

$$\hat{\mathcal{P}}_{\text{tot}} = -\frac{1}{4} \int_0^{L_y} \left[\int_{L_x}^{L_x + \Delta_{\text{sh}}} \left(J_x^{(\text{sh})} \frac{\partial \Phi_\omega^{(\text{sh})*}}{\partial x} + J_x^{(\text{sh})*} \frac{\partial \Phi_\omega^{(\text{sh})}}{\partial x} \right) dx \right] dy. \quad (\text{C.3})$$

The integration with respect to x can be easily performed by noting that $J_x^{(\text{sh})}$ is constant over the sheath when both the particle and displacement currents are included [25]. Using the definition of the RF sheath voltage V_{RF} (see Eq. (3)), we obtain

$$\hat{\mathcal{P}}_{\text{tot}} = \frac{1}{4} \int_0^{L_y} (J_x^{(\text{sh})} V_{\text{RF}}^* + J_x^{(\text{sh})*} V_{\text{RF}}) dy. \quad (\text{C.4})$$

Substituting Eq. (4) into Eq. (C.4) (noting that $J_n^{(\text{sh})} \rightarrow -J_x^{(\text{sh})}$) yields

$$\hat{\mathcal{P}}_{\text{tot}} = \frac{1}{2} \int_0^{L_y} |J_x^{(\text{sh})}|^2 \text{Re}(z_{\text{sh}}) dy = \int_0^{L_y} P dy, \quad (\text{C.5})$$

where P is the local power density defined in Section 5.1.

Second, we consider another expression for the total sheath power dissipation by employing Poynting's theorem

$$\nabla \cdot \langle \mathbf{S} \rangle + \langle \mathbf{J} \cdot \mathbf{E} \rangle = 0, \quad (\text{C.6})$$

where $\mathbf{S} = \mathbf{E} \times \mathbf{B}/\mu_0$ is the Poynting vector, and the time average of the product of A and B is defined by $\langle AB \rangle = (A^*B + AB^*)/4$. Integrating Eq. (C.6) over the entire sheath region and using the definition (C.1) yields

$$\mathcal{P}_{\text{tot}} = - \int_{\text{sheath}} \nabla \cdot \langle \mathbf{S}^{(\text{sh})} \rangle dV. \quad (\text{C.7})$$

Then, with the use of Gauss' theorem, the power density per unit length, $\hat{\mathcal{P}}_{\text{tot}}$, corresponding to Fig. 5 is given by

$$\hat{\mathcal{P}}_{\text{tot}} = \int_0^{L_y} \langle S_x^{(\text{sh})} \rangle dy \Big|_{x=L_x}. \quad (\text{C.8})$$

Note that $\langle S_x^{(\text{sh})} \rangle = 0$ on the surface of the metal wall at $x = L_x + \Delta_{\text{sh}}$ (due to the conducting-wall BC). Consequently, substituting $S_x^{(\text{sh})} = (E_y^{(\text{sh})} B_z^{(\text{sh})} - E_z^{(\text{sh})} B_y^{(\text{sh})}) / \mu_0$ into Eq. (C.8) and using the continuity of \mathbf{E} and \mathbf{B} at the sheath-plasma interface, we obtain

$$\hat{\mathcal{P}}_{\text{tot}} = \int_0^{L_y} \langle S_x \rangle dy \Big|_{x=L_x} = \frac{1}{2\mu_0} \int_0^{L_y} \text{Re} (E_y B_z^* - E_z B_y^*) dy \Big|_{x=L_x}. \quad (\text{C.9})$$

Here, $\langle S_x \rangle$ and the components of \mathbf{E} and \mathbf{B} are the quantities on the plasma side.

Although the integrated values in Eqs. (C.5) and (C.9) must be the same, the local power density P and the local time-averaged Poynting vector component $\langle S_x \rangle$ on the sheath surface are different in general. This can be confirmed by the following relation:

$$P = \langle S_x \rangle|_{x=L_x} - \frac{d}{dy} \int_{L_x}^{L_x + \Delta_{\text{sh}}} \langle S_y^{(\text{sh})} \rangle dx. \quad (\text{C.10})$$

Fig. C.17 shows the plot of P and $\langle S_x \rangle$ as functions of y at the sheath-plasma interface ($x = L_x$) for $n_0 = 1 \times 10^{17} \text{ m}^{-3}$ and $k_z = 320 \text{ m}^{-1}$ under the generalized sheath BC, which corresponds to the result at $K_{\text{max}} = 10 \text{ A/m}$ in Section 5.1. Here, the magnetic flux density at node i in the domain Ω , which is denoted by \mathbf{B}_i , is calculated using the following nodal averaging technique after the converged solution is obtained (see Eq. (5) for the definition of N_i):

$$\mathbf{B}_i = \frac{1}{i\omega} \frac{\int_{\Omega} N_i \nabla \times \mathbf{E} d\Omega}{\int_{\Omega} N_i d\Omega}. \quad (\text{C.11})$$

It is seen that these profiles do not overlap each other. However, the integrated values of P and $\langle S_x \rangle$ in the range $0 \leq y \leq L_y$ are 2.958×10^{-2} and $2.961 \times 10^{-2} \text{ kW/m}$, respectively, which indicates that the numerical result obtained by the new rfSOL code well satisfies the required condition for $\hat{\mathcal{P}}_{\text{tot}}$.

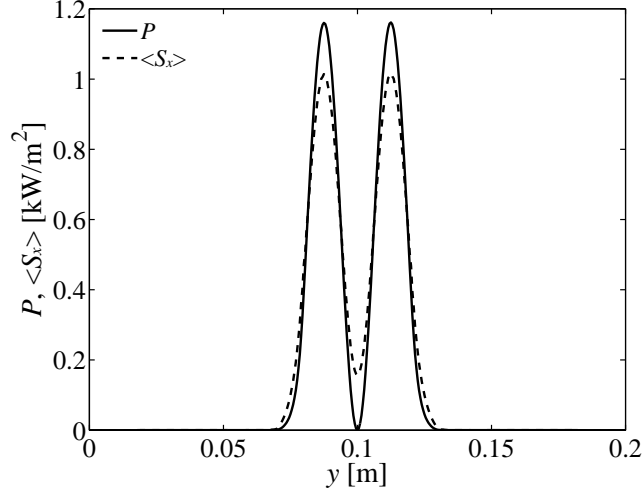


Figure C.17: Comparison of the profiles of P and $\langle S_x \rangle$ along the sheath surface for $n_0 = 1 \times 10^{17} \text{ m}^{-3}$ and $k_z = 320 \text{ m}^{-1}$ at $K_{\text{max}} = 10 \text{ A/m}$, which are obtained using the generalized sheath BC.

Appendix D. Sheath-plasma wave in the capacitive sheath model

In Section 5.3, we notice the presence of the SPW when the capacitive sheath BC is used. Here, we derive the conditions for the SPW in electromagnetic theory, which can be used to interpret the numerical results in Section 5.3.

Since we assume that the direction of the background magnetic field \mathbf{B}_0 is perpendicular to the sheath surface, the capacitive sheath BC shown in Eq. (24) can be rewritten as

$$E_{\perp} = ik_{\perp} \Delta_{\text{sh}} b_n \varepsilon_{\parallel} E_{\parallel}, \quad (\text{D.1})$$

where the subscripts \perp and \parallel denote the components perpendicular and parallel to \mathbf{B}_0 , respectively, and we note that $b_n = -1$ at $x = L_x$ in Fig. 5. For the electromagnetic SW, the relationship between the electric field components is given by

$$E_{\perp} = -\frac{n_{\perp} n_{\parallel}}{\varepsilon_{\perp} - n_{\parallel}^2} E_{\parallel}. \quad (\text{D.2})$$

A condition for the SPW is obtained by combining Eqs. (D.1) and (D.2) (to

eliminate E_{\perp} and E_{\parallel}) as follows:

$$i = \frac{\varepsilon_{\perp} - n_{\parallel}^2}{n_{\parallel}} \frac{\Delta_{\text{sh}} \omega}{c} b_n \varepsilon_{\parallel}. \quad (\text{D.3})$$

In addition, at the sheath-plasma interface, we obtain the following expression of n_{\perp}^2 from the electromagnetic SW dispersion relation:

$$n_{\perp}^2 = \frac{\varepsilon_{\parallel}}{\varepsilon_{\perp}} (\varepsilon_{\perp} - n_{\parallel}^2). \quad (\text{D.4})$$

The condition $n_{\perp}^2 > 0$ is required for the SPW to propagate along the sheath surface, while the condition $n_{\parallel}^2 < 0$ is required for the SPW to be evanescent away from the wall. These two conditions are satisfied when $|n_{\parallel}^2| > |\varepsilon_{\perp}|$, since $\varepsilon_{\parallel} < 0$ and $\varepsilon_{\perp} < 0$ for a high-density plasma. Further, for the simulations which have the sheath at the right wall, the sign of $\text{Im}(n_{\parallel})$ needs to be negative, i.e., $n_{\parallel} = -i|n_{\parallel}|$ (or $k_{\parallel} = -i|k_{\parallel}|$), considering that the modes vary as $e^{ik_x x} \sim e^{|k_{\parallel}|x}$. Thus, from Eq. (D.4) we obtain

$$n_{\parallel} = -i \left| \frac{\varepsilon_{\perp}}{\varepsilon_{\parallel}} (\varepsilon_{\parallel} - n_{\perp}^2) \right|^{1/2}. \quad (\text{D.5})$$

Substituting Eq. (D.5) and $b_n = -1$ into Eq. (D.3) yields

$$1 = \Delta_{\text{sh}}^2 k_{\perp}^2 n_{\perp}^2 \frac{\varepsilon_{\perp} \varepsilon_{\parallel}}{n_{\perp}^2 - \varepsilon_{\parallel}}. \quad (\text{D.6})$$

This expression can be rewritten in the form of a quadratic equation for k_{\perp}^2 . After taking the positive root of the quadratic equation (due to $n_{\perp}^2 > 0$), the y component of the wave vector of the SPW, $k_{\text{SPW},y}$, is given by

$$k_{\text{SPW},y} = (k_{\perp}^2 - k_z^2)^{1/2}. \quad (\text{D.7})$$

The positive real root of Eq. (D.7) with the parameters used in Section 5.3 is plotted in Fig. 16, as denoted by a solid curve.

References

- [1] M.A. Lieberman, A.J. Lichtenberg, Principles of Plasma Discharges and Materials Processing, second edition, Wiley-Interscience, 2005.

- [2] E.F. Jaeger, L.A. Berry, J.S. Tolliver, D.B. Batchelor, *Phys. Plasmas* 2 (1995) 2597–2604.
- [3] M.D. Carter, P.M. Ryan, D. Hoffman, W.S. Lee, D. Buchberger, V Godyak, *J. Appl. Phys.* 100 (2006) 073305.
- [4] T.G. Jenkins, D.N. Smithe, *Plasma Sources Sci. Technol.* 24 (2015) 015020.
- [5] J.R. Myra, D.A. D’Ippolito, *Plasma Phys. Control. Fusion* 52 (2010) 015003.
- [6] L. Colas, J. Jacquot, S. Heuraux, E. Faudot, K. Crombé, V. Korytsya, J. Hillairet, M. Goniche, *Phys. Plasmas* 19 (2012) 092505.
- [7] S.J. Wukitch, M.L. Garrett, R. Ochoukov, J.L. Terry, A. Hubbard, B. Labombard, C. Lau, Y. Lin, B. Lipschultz, D. Miller, M.L. Reinke, D. Whyte, Alcator C-Mod Team, *Phys. Plasmas* 20 (2013) 056117.
- [8] D. Van Eester, K. Crombé, V. Korytsya, *Plasma Phys. Control. Fusion* 55 (2013) 055001.
- [9] D.A. D’Ippolito, J.R. Myra, R. Ochoukov, D.G. Whyte, *Plasma Phys. Control. Fusion* 55 (2013) 085001.
- [10] J. Jacquot, D. Milanesio, L. Colas, Y. Corre, M. Goniche, J. Gunn, S. Heuraux, M. Kubič, *Phys. Plasmas* 21 (2014) 061509.
- [11] R. Ochoukov, D.G. Whyte, D. Brunner, D.A. D’Ippolito, B. LaBombard, B. Lipschultz, J.R. Myra, J.L. Terry, S.J. Wukitch, *Plasma Phys. Control. Fusion* 56 (2014) 015004.
- [12] D.N. Smithe, D.A. D’Ippolito, J.R. Myra, *AIP Conference Proceedings* 1580 (2014) 89–96.
- [13] J.R. Wilson, P.T. Bonoli, *Phys. Plasmas* 22 (2015) 021801.
- [14] R.J. Perkins, J.C. Hosea, M.A. Jaworski, J.-W. Ahn, A. Diallo, R.E. Bell, N. Bertelli, S. Gerhardt, T.K. Gray, G.J. Kramer, B.P. LeBlanc, A. McLean, C.K. Phillips, M. Podestà, L. Roquemore, S. Sabbagh, G. Taylor, J.R. Wilson, *Phys. Plasmas* 22 (2015) 042506.

- [15] T.G. Jenkins, D.N. Smithe, AIP Conference Proceedings 1689 (2015) 030003.
- [16] H. Kohno, J.R. Myra, D.A. D’Ippolito, Phys. Plasmas 22 (2015) 072504;
H. Kohno, J.R. Myra, D.A. D’Ippolito, Phys. Plasmas 23 (2016) 089901,
Erratum.
- [17] V. Bobkov, F. Braun, R. Dux, A. Herrmann, H. Faugel, H. Fünfgelder,
A. Kallenbach, R. Neu, J.-M. Noterdaeme, R. Ochoukov, Th. Pütterich,
A. Tuccilo, O. Tudisco, Y. Wang, Q. Yang, ASDEX Upgrade team,
Nucl. Fusion 56 (2016) 084001.
- [18] L. Colas, L.-F. Lu, A. Křivská, J. Jacquot, J. Hillairet, W. Helou, M. Go-
niche, S. Heuraux, E. Faudot, Plasma Phys. Control. Fusion 59 (2017)
025014.
- [19] K. Crombe, R. D’Inca, J. Jacquot, R. Ochoukov, M. Usoltceva, A. Kos-
tic, F. Louche, D. Van Eester, A. Nikiforov, J. Moreno, S. Heuraux,
S. Devaux, J. Moritz, E. Faudot, H. Fünfgelder, H. Faugel, F. Zeus, J.-
M. Noterdaeme, 26th IAEA Fusion Energy Conf. (Kyoto, Japan, 17–22
October 2016) IAEA-CN-234/EX/P6-48.
- [20] M. Martin, W. Gekelman, P. Pribyl, B. Van Compernelle, T. Carter,
D. Van Eester, K. Crombé, Bull. Amer. Phys. Soc. 61 (2016) 299, paper
PP10-11.
- [21] J.R. Myra, D.A. D’Ippolito, M. Bures, Phys. Plasmas 1 (1994) 2890–
2900.
- [22] D.A. D’Ippolito, J.R. Myra, Phys. Plasmas 13 (2006) 102508.
- [23] H. Kohno, J.R. Myra, D.A. D’Ippolito, Comput. Phys. Comm. 183
(2012) 2116–2127.
- [24] H. Kohno, J.R. Myra, D.A. D’Ippolito, Phys. Plasmas 19 (2012) 012508.
- [25] J.R. Myra, D.A. D’Ippolito, Phys. Plasmas 22 (2015) 062507.
- [26] J.R. Myra, H. Kohno, 26th IAEA Fusion Energy Conf. (Kyoto, Japan,
17–22 October 2016) IAEA-CN-234/TH/P4-31.
- [27] C.D. Child, Phys. Rev. (Series I) 32 (1911) 492–511.

[28] I. Langmuir, Phys. Rev. 21 (1923) 419–435.

[29] T.H. Stix, Waves in Plasmas, American Institute of Physics, 1992.